Chemical Science

ROYAL SOCIETY OF CHEMISTRY

REVIEW

View Article Online
View Journal | View Issue

Cite this: *Chem. Sci.*, 2024, **15**, 14585

Spin effect in dual-atom catalysts for electrocatalysis

Xiaoqin Xu and Jingqi Guan *

The development of high-efficiency atomic-level catalysts for energy-conversion and -storage technologies is crucial to address energy shortages. The spin states of diatomic catalysts (DACs) are closely tied to their catalytic activity. Adjusting the spin states of DACs' active centers can directly modify the occupancy of d-orbitals, thereby influencing the bonding strength between metal sites and intermediates as well as the energy transfer during electro reactions. Herein, we discuss various techniques for characterizing the spin states of atomic catalysts and strategies for modulating their active center spin states. Next, we outline recent progress in the study of spin effects in DACs for the oxygen reduction reaction (ORR), oxygen evolution reaction (OER), hydrogen evolution reaction (HER), electrocatalytic nitrogen/nitrate reduction reaction (eNRR/NO_3RR), and electrocatalytic carbon dioxide reduction reaction (eCO_2RR) and provide a detailed explanation of the catalytic mechanisms influenced by the spin regulation of DACs. Finally, we offer insights into the future research directions in this critical field.

Received 2nd July 2024
Accepted 19th August 2024

DOI: 10.1039/d4sc04370g

rsc.li/chemical-science

1. Introduction

The growing consumption of fossil fuels and serious climate change seriously hinder the sustainable development of human society, prompting researchers to seek effective strategies to deal with them.[1,2] Renewable energy-conversion technologies involve various chemical transformation processes, providing a sustainable and green route to relieve these urgent issues.[3,4] Among these technologies, electrochemical conversion processes, such as fuel cells and Zn–air batteries (involving the ORR and OER), water splitting (involving the OER and HER), and eCO_2RRs and eNRRs/eNO_3RRs, which can facilitate the transformation of H_2O, CO_2, and N_2 in the atmosphere into high-value-added products through coupling with renewable energy, represent a promising avenue for the development of sustainable energy solutions.[5–7] Catalysts play a crucial role in energy-conversion techniques, with more than 80% of industrial processes utilizing catalysts to improve the speed, efficiency, and selectivity of reactions.[8] Currently, precious metal catalysts (such as Pt, Au, Ru, and Ir) generally perform better than non-noble metal materials in facilitating electrocatalytic reaction kinetics. However, the limited supply and high cost of precious metals have greatly prevented them from being used on a large scale commercially.[9] Therefore, powerful and cost-effective metal-based (TM) catalysts are needed to help the chemical industry to move toward a more sustainable future.

Most catalytic processes occur on the metal surface, resulting in low catalyst utilization and limiting the catalytic performance. An effective strategy to improve metal utilization is downsizing catalysts and reducing the size of the active metal in solid metal catalysts to the atomic level to form single-atom catalysts (SACs), as proposed by Zhang *et al.* in 2011,[10] thus making full use of metal atoms.[11–13] Apart from maximized atomic utilization, SACs possess the advantages of uniform active sites, and the way their electronic structure and unsaturated coordination environment work together can improve the performances of various catalytic reactions.[14,15] Although SACs show great prospects in catalysis, there are various limitations in this class of single-atom structures, such as low metal loading, only one type of specific active sites, and relatively weak interaction, which hinder their development.[16,17] The advent of bimetallic nanocatalysts has led to the development of DACs, which have been considered a promising extension of SACs that can address the aforementioned challenges. DACs comprise isolated pairs of metal atoms, which act as the active sites. In homonuclear DACs, the same metal is present, whereas in heteronuclear DACs, different metals are present.[18] In the 1980s, Muetterties *et al.* documented the semi-hydrogenation of internal alkynes to *trans*- or (*E*)-isomers using di-nuclear rhodium organic compounds, which was one of the earliest instances of catalytic reduction utilizing a synthetic DAC.[19] DACs have many advantages over SACs, including: (1) the dual metal sites exhibit greater flexibility, enabling them to optimize the adsorption energy of specific intermediates and break the linear progression relationship;[20] (2) the tunable electronic structure and spin states of DACs facilitate an enhancement of

Institute of Physical Chemistry, College of Chemistry, Jilin University, Changchun 130021, PR China. E-mail: guanjq@jlu.edu.cn

the ORR/OER kinetics, thus improving the energy-conversion efficiency and the cycle life of the associated energy-storage devices; thus paving the way for future practical applications of DACs;[21] (3) DACs have a greater potential to adjust the d-band center through interactions of the electronic orbits compared SACs; thus allowing tuning the binding energy of the intermediates at the catalytic sites.[1,22]

The initiation of chemical reactions depends on two essential factors: the energies involved (both free and activation energies) and the angular momentum (spin) of the reactants.[23] Since water oxidation, fuel cell reactions, and CO_2 conversion involve transitions between triplet and singlet states or the participation of radicals, the influence of electron spin dynamics in these reactions cannot be ignored. Recent research has shown that the spin states (low, medium, and high spins) or magnetic structures of the active centers in DACs can directly influence the reaction barriers of catalytic reactions by adjusting the bonding of the reaction intermediates species with catalytic sites, as the formation energies of singlet products are generally higher than those of triplet ground-state products.[24–26] Furthermore, the majority of DACs with unpaired spin electrons invariably demonstrate spin-dependent magnetism, filtering effective spin electrons through the magnetic field and thus effectively accelerating spin-dependent electrocatalytic reactions.[27] Besides the influence of magnetism, other factors can affect the spin of electrons, such as the crystal field, coordination environment, oxidation state, bonding characteristics, electron count, and conductivity.[28]

The spin effect has been applied to the whole catalytic system; however, there is currently no reports providing a systematic summary of the spin effect in DACs. Consequently, this review highlights recent progress in the discovery of the influence of electron spin in DACs on the electrocatalysis of the HER, OER, ORR, CO_2RR, and eNRR/eNO_3RR, with a primary development schedule shown in Fig. 1 highlighting the major steps in the progress in DACs research. The concept of the spin effect was first introduced by Compton *et al.* in 1921,[29] marking the beginning of its development in the context of electrocatalysts. It was not until the 1980s that binuclear molecules were first proposed and diatomic catalysts began to emerge as a prominent area of study.[30] Subsequently, the study of DACs advanced from their initial preparation and modulation to an examination of the synergistic impact of charge iteration and electron spin polarization, which broadened the potential applications of DACs.[33] Despite remaining in its infancy, the findings emerging from the investigation of the spin effect of DACs have attracted significant interest across various catalytic domains. This examination focuses on a detailed analysis of the crucial roles of the electron properties, specifically charge and spin, in these reactions. Additionally, we summarize strategies for optimizing the catalytic efficiency by manipulating these properties. We systematically discuss the physical and electrochemical properties of electrons and spin, and their interactions with reactants and intermediates. This review addresses the challenges and opportunities in developing high-performance catalysts, concluding with a forward-looking exploration of the future of spin catalysis.

2. Fundamentals of spin

The spin of the electron is an important fundamental property, which arises from its internal angular momentum, and plays a crucial role in manipulating various aspects of catalysis. In the context of quantum mechanics, the co-localization of two electrons in the same orbital is possible only if they possess opposite spins.[38] The state in which an electron spins in an atomic or molecular orbital is called a spin state. Following the interaction, the five sub-d-orbitals split into a low-energy t_{2g} bonding orbital that includes d_{xy}, d_{yz}, and d_{xz} and a high-energy e_g antibonding orbital that includes $d_{x^2-y^2}$ and d_{z^2}, as demonstrated in Fig. 2.[33,39] Fission energy ($\Delta 0$) is an important concept, which is the difference in energy levels between e_g and t_{2g} orbitals. Another important concept is the electron pairing energy (P), which is the energy needed to pair electrons with opposite spins within the same orbital. The degree of spin polarization is determined by the relative values of these two energies: when $\Delta 0$ exceeds P, electrons tend to preferentially occupy the triple degenerate t_{2g} orbitals, which are associated with the low-spin state in a strong field. Conversely, the electrons occupy the orbits in accordance with the analogous Hunt rule, designated as the high-spin state in a weak field.[39] Under specific conditions, the electron spin states in atoms or molecules align in a particular direction, a phenomenon known as spin polarization.[40] Moreover, the radical-pair mechanism was initially proposed by Closs and independently identified by Lawler in 1969.[41] In chemical reactions, due to the selection rules, reaction is prohibited if a change in spin is required.[42] More and more scientists have realized that modulating the electron spin properties is a feasible means to heighten the intrinsic activity of catalysts, and thus the concept of spin catalysis has emerged.[43] Since the specific mechanism of the spin effect in different electrocatalytic reactions varies, understanding the spin of metals is important for the design of DACs with enhanced electrocatalytic activities. This section begins with an introduction to the descriptors, the catalytic mechanism, and the regulation method of spin polarization for electrocatalytic reactions.

2.1. Catalytic descriptors based on spin polarization

In recent years, more and more researchers have combined experimental results with theoretical calculations to enhance the comprehension of electrocatalytic processes. Therefore, the descriptors derived from theoretical aspects play a significant role using the physical and chemical properties of an electrocatalyst as an indicator of its electrocatalytic activity in the electrocatalytic process.[44] In this section, we discuss the development of descriptors that correlate the electrocatalytic activity of electrocatalysts, especially DACs, with spin polarization.

2.1.1. Magnetic fields. The spin effect is intimately associated with the phenomenon of magnetism, thus the utilization of magnetic fields represents a significant methodology for the regulation of the spin in DACs. The transmission of high-intensity energy by magnetic fields can result in alterations to the configuration of spin electrons situated outside the nucleus.

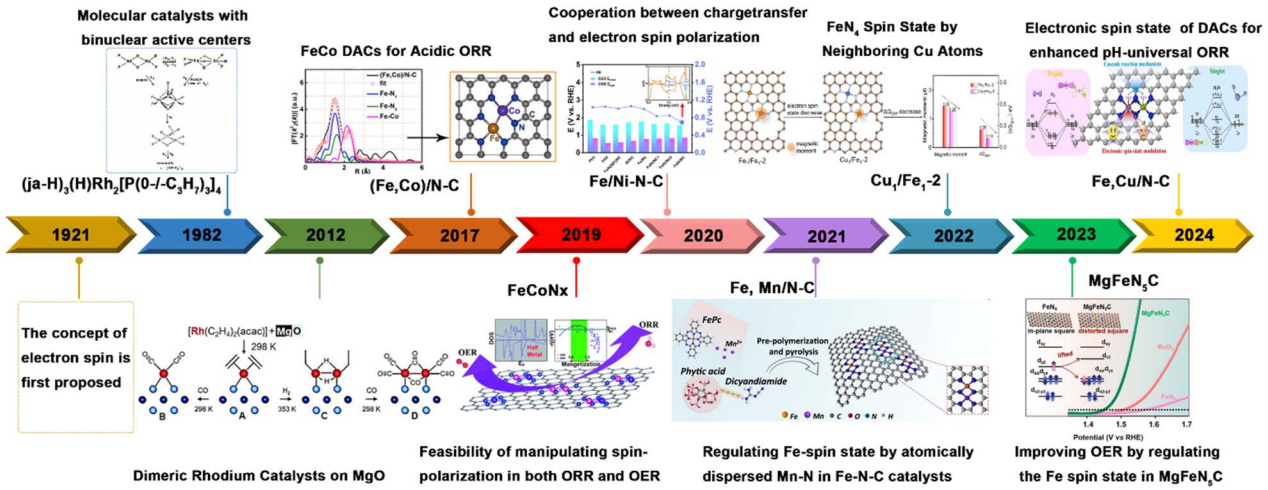

Fig. 1 History of DACs with spin regulation for electrocatalysis, including the concept of electron spin. Reproduced with permission.[29] Copyright 1921, Elsevier. Also shown are some representative DACs: $(ja\text{-}H)_3(H)Rh_2[P(0\text{-}/\text{-}C_3H_7)_3]_4$. Reproduced with permission.[19] Copyright 1982, American Chemical Society. Dimeric Rh catalysts on MgO. Reproduced with permission.[30] Copyright 2012, Wiley-VCH. (Fe, Co)/N–C. Reproduced with permission.[31] Copyright 2017, American Chemical Society. $FeCoN_x$. Reproduced with permission.[32] Copyright 2019, Royal Society of Chemistry. Fe/Ni–N–C. Reproduced with permission.[33] Copyright 2021, Elsevier. Fe, Mn/N–C. Reproduced with permission.[34] Copyright 2021, Nature. Cu_1/Fe_1-2. Reproduced with permission.[35] Copyright 2022, Wiley-VCH. $MgFeN_5C$. Reproduced with permission.[36] Copyright 2023, Wiley-VCH. and Fe, Cu/N–C. Reproduced with permission.[37] Copyright 2024, Elsevier.

This phenomenon gives rise to changes in the arrangement, coordination, and motion of atoms, molecules, and ions.[45] This phenomenon is a consequence of the charge motions, endowing elementary particles with magnetic moments. Two principal aspects of how magnetic field-induced spin selectivity affects electrocatalytic processes warrant consideration. On the one hand, spin flipping can result in the adsorption of intermediates on the catalyst surface, thereby enhancing the reaction pathway and increasing the reaction efficiency. Alternatively, the magnetic field can facilitate the transition of spin-related radicals between two spin states (singlet or triplet) to yield distinct products, thereby influencing the efficiency of the

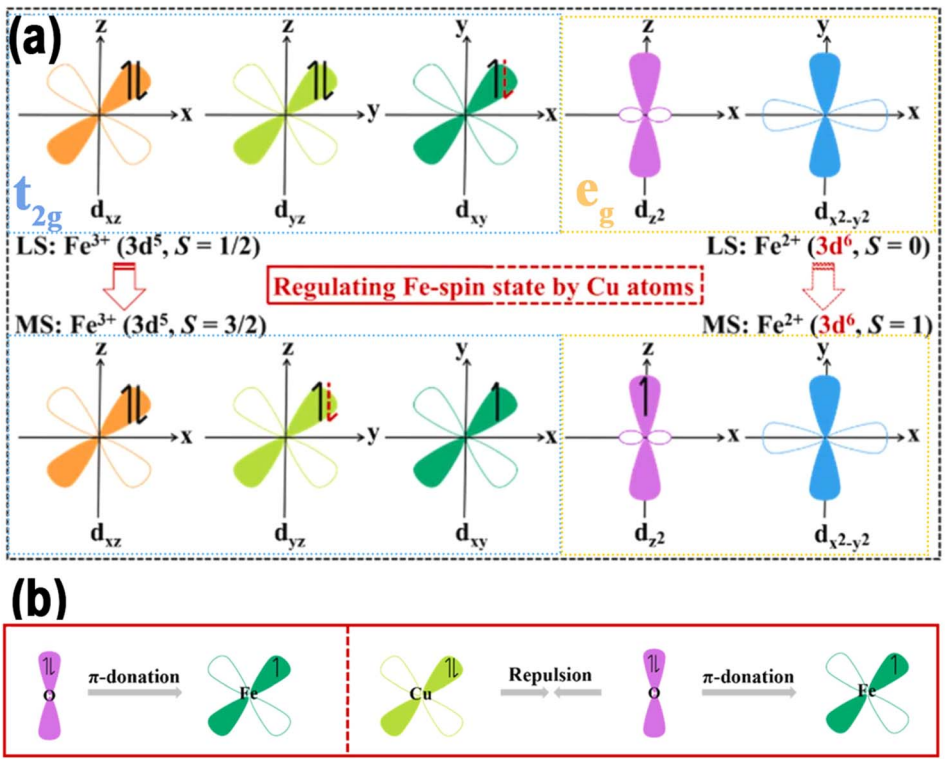

Fig. 2 (a) Five d-orbitals in Fe, Cu/N–C. (b) Scheme of d_{xy} electron interaction in Fe/N–C and Fe, Cu/N–C. Reproduced with permission.[37] Copyright 2024, Elsevier.

electrocatalytic process.[46–48] In the context of electrocatalysis, the term "magnetic fields" encompasses two distinct types: external magnetic fields, which are additional magnetic fields applied by external machinery or devices, and internal magnetic fields, which are generated by the magnetic catalyst itself.[25]

2.1.2. Electronic spin moments. Electron spin creates a magnetic moment, referring to a tiny magnetic dipole moment. Both spin-polarized electrons and radical molecules generate magnetic moments, and thus, external magnetic fields can be strategically used to control spin states and thereby influence the reaction kinetics.[49] Numerous studies have demonstrated that the spin magnetic moment is related to the adsorption sites at TM atoms,[50] and can be used as a structural–activity relationship descriptor for Fe-based SACs.[51] For example, Zhong *et al.* used density functional theory calculation (DFTs) to calculate the ORR catalyzed by C_2N-loaded Fe SAs (C_2N-Fe). The near linear correlation observed between variations in the spin moment and the catalytic activity indicates that the electronic spin magnetic moment is a hopeful descriptor for Fe-based SACs.[51] Zhang *et al.* revealed the electron spin construction of Fe, Mn/N–C by measuring the temperature-dependent magnetic susceptibility. The computed magnetic moments of Fe and Mn/N–C (3.75 μ_{eff}) were longer than the available magnetic moments of Fe/N–C, as shown in Fig. 3a and b.[34] Moreover, a higher magnetic moment or spin moment may affect the catalytic performance, because such electronic properties could provide a convenient electronic spin-selective transmission channel.[56] Recently, Ma *et al.* theoretically demonstrated the presence of ultra-high density DACs with metal loads higher than 40 wt% and revealed that the spin magnetic moment of the active centers can act as an ORR catalytic descriptor, as depicted in Fig. 3c.[52]

2.1.3. D-band center gap. The d-band center is an important descriptor in catalysis, and its energy level determines the stability and strength of adsorption bond formation. The d-band model of adsorption can clarify how the regulation of the magnetic metal surface's spin state has a significant impact on the chemical features.[57] For instance, Liu *et al.* proved that the d-band center gap of the Fe spin state (Δd) is related to the ORR activity of the Fe–N_4 site, and the fitting results between Δd and the free energy difference (ΔG) indicated that Δd is a hopeful descriptor for the ORR activity, as shown in Fig. 3d.[53]

2.1.4. Spin density. Recent reports have shown that spin density can influence the rate-determination step to adjust the catalytic activity, which can be used as a descriptor of spin catalysis.[58] Xia *et al.* found an active catalytic site with a high positive spin density and high positive charge density on mono-nitrogen-doped graphene in 2011. They demonstrated that N-doping could make the spin density and atomic charge density asymmetric, which made N-GO exhibit excellent electrocatalytic ORR activity.[59] Modulation of the spin density at the center of a single atom has encyclopedic essential meaning and technical implications for understanding single-atom catalysis. For example, a criterion for creating high-efficiency magnetic SACs for sustainable energy transformation was developed by Lu *et al.* using spin–activity correlations.[54] Experimental and theoretical results displayed that the spin density-dependent OER activity of single Co atoms adsorbed at hollow sites (CoHS) was optimal in the presence of hetero-single CoTa sites, in contrast to homo-single CoHS sites that produce excessive spin density in the presence of nearby CoHS. The spin density was further used as a descriptor to evaluate the spin polarization in DACs, demonstrating significant spin polarization at the Fe site in $FeNiN_6$-DAC through spatial spin density analysis (Fig. 3e). This analysis revealed that the high charge transfer enhances OH* desorption, leading to H_2O release, thereby positioning this configuration as a promising ORR catalyst.[60]

2.1.5. Adsorption energies of key reaction intermediates. Since the regulation of the electron spin state of the active center of 3d metals can directly affect the adsorption behavior of DACs with key reaction intermediates, the reaction free energy can be used as a catalytic reaction descriptor.[14] To analyze the possible relationship between the selectivity or activity of DACs for the CO_2RR and the adsorption properties of key active intermediates, Li *et al.* took the adsorption energy of the key reaction intermediates *COOH, *HCOOH, *CO, and *OCHO as effective descriptors for predicting additional reaction information from van der Waals spin-polarized density functional calculations, and established a linear scale relationship between them, as shown in Fig. 3f–h.[55]

2.2. Spin state characterizations

An invaluable approach to the modulation of electronic structures is the induction of spin state transitions. This procedure demands different characterization techniques to measure the electron occupancy in t_{2g} and e_g orbitals. In this section, we detail the analytical methods used in the characterization techniques.

2.2.1. Vibrating sample magnetometry (VSM). VSM is an essential technique for characterizing the magnetic properties of materials. This high-sensitivity technique operates based on electromagnetic induction principles. The magnetic moment of a sample is directly proportional to the induced voltage in the detection coil in the VSM instrument, the amplitude of vibration, and the frequency of vibration.[61,62] By using a lock-in amplifier to measure the voltage while maintaining constant amplitude and vibration frequency, the magnetic moment of the sample can be calculated. VSM is capable of identifying the inherent magnetic characteristics of diverse materials, such as the saturation magnetization (M_s or σ_s), Curie temperature (T_f), coercivity (H_c), and remanence (M_r).[63] It can provide magnetization *vs.* magnetic field (M–H) splines or magnetic moment *vs.* temperature (M–T) splines, allowing the calculation of a material's effective magnetic moment (μ_{eff}).[64] In catalyst design, the number of unpaired electrons at the active centers can be confirmed from this μ_{eff}, thereby allowing inferring the spin state of the material.[65] For example, Wang *et al.* enhanced the rate-determining step (RDS) of the OER kinetics by tuning the electronic spin of mono-dispersed Fe active sites.[66] To obtain a more detailed insight of the electronic structure of $Fe_{SA/AC}$@HNC, hysteresis loops were collected at room temperature. As depicted in Fig. 4a, the saturation magnetization increased from 8.4 emu g^{-1} to 114.8 emu g^{-1}. The inset in Fig. 4a provides

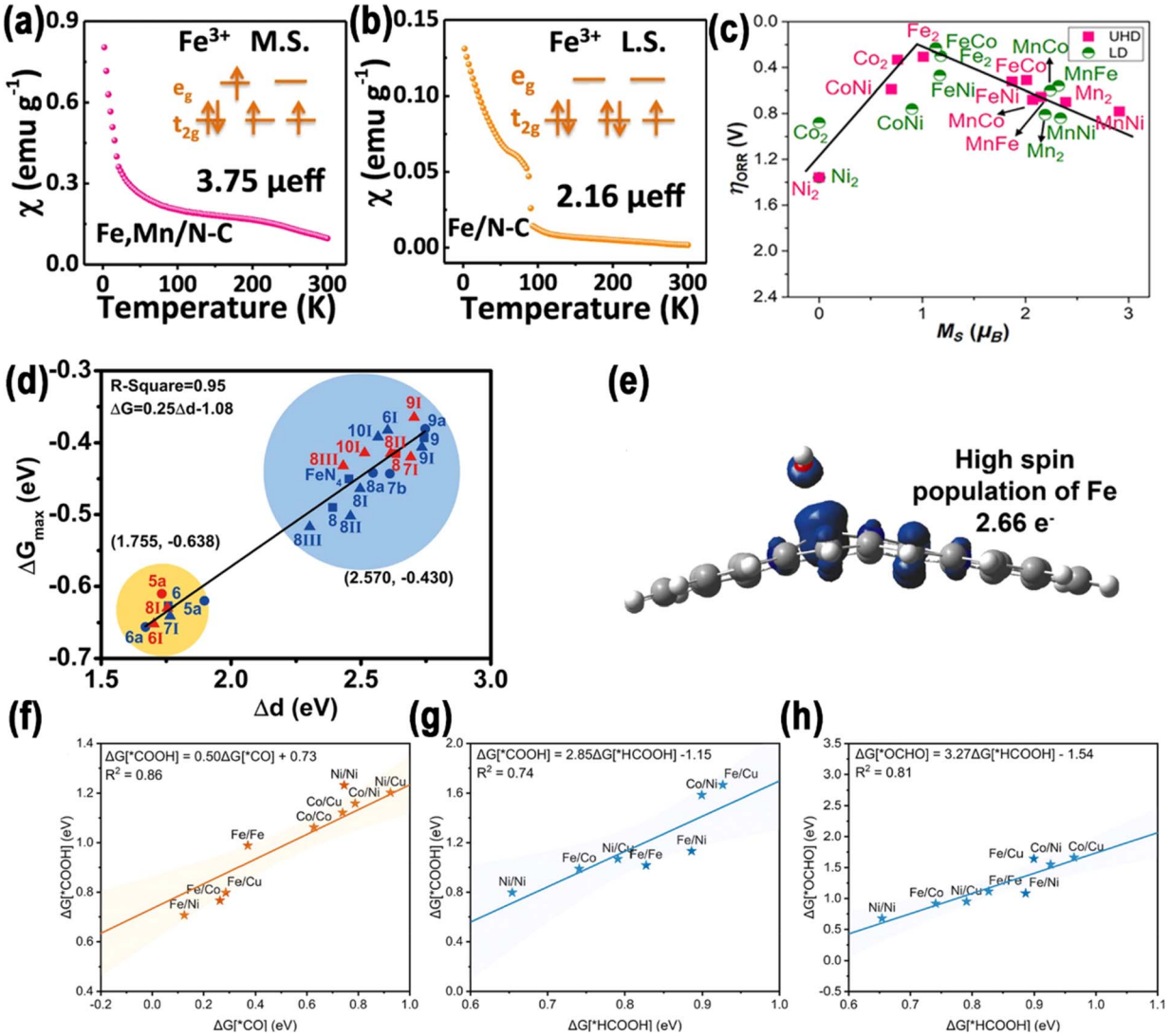

Fig. 3 (a) Zero-field cooling temperature-dependent magnetic susceptibility of Fe, Mn/N–C, (b) Fe/N–C. Reproduced with permission.[34] Copyright 2021, Nature. (c) Volcano plots illustrating the relationship between the local spin magnetic moments of metal atoms, with the optimal pathway for *OH anchoring presented. Reproduced with permission.[52] Copyright 2023, American Chemical Society. (d) Correlation between Δd and ΔG. Reproduced with permission.[53] Copyright 2022, Nature. (e) Charge transfer in $FeNiN_6$-DAC. Reproduced with permission.[54] Copyright 2021, American Chemical Society. Comparisons of the binding energies between (f) *COOH and *CO, (g) *OCHO and *HCOOH, as well as (h) *COOH and *HCOOH. Reproduced with permission.[55] Copyright 2023, American Chemical Society.

an enlarged view near $H = 0$, indicating a coercivity (H_c) of 273.3 Oe and a remanent magnetization (M_r) of 16.6 emu g^{-1} for Fe_{SA}/AC@HNC, exceeding those of Fe_{SA}@HNC. The above evidence combined with the results of zero-field cooling temperature-dependent (ZFC-T) magnetic susceptibility (χ_m) measurements strongly indicated that incorporating Fe clusters alters the Fe–N_4 spin state by increasing the number of unpaired electrons. In addition, Wang *et al.* measured the *M*–*T* of PQD-Fe and o-MQFe-10 : 20 : 5 to investigate the spin state of Fe(III).[67] The *M*–*T* tests showed that PQD-Fe and o-MQFe-10 : 20 : 5 had μ_{eff} values of 1.69 μ_B and 3.65 μ_B, with unpaired electron numbers of 0.96 and 2.78, respectively (Fig. 4b).

2.2.2. Electron paramagnetic resonance (EPR). EPR is a magnetic resonance technique that can be used to characterize materials by utilizing the resonance absorption properties of substances with unpaired electrons in a static magnetic field. This method can be used for both the qualitative and quantitative detection of unpaired electrons in both atoms and molecules, as well as to investigate the structural attributes of the surrounding environment.[72] By analyzing EPR spectra, it is possible to study the spin–lattice relaxation, spin–spin coupling, and spin–orbit coupling in paramagnetic substances. In energy catalysis, EPR technology is often used to analyze the spin states and coordination conditions of catalysts. When the electron spins in the sample couple through antiferromagnetic interactions, causing the spin vectors to align antiparallel and resulting in a total spin of zero, the EPR signal disappears.[73] For example, Li *et al.* adjusted the spin state of Fe in Fe–N–C (from high to intermediate) to enhance nitrogen-fixation activity by introducing an S atom coordination.[68] As shown in Fig. 4c, EPR

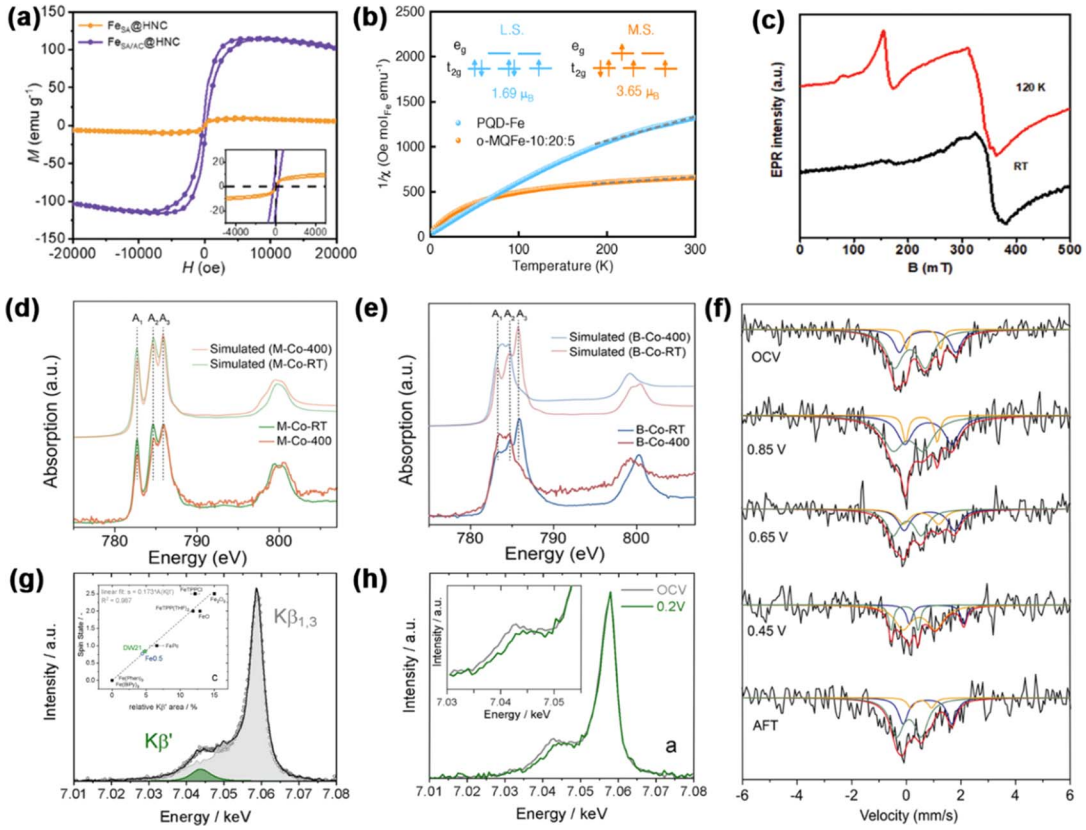

Fig. 4 (a) Magnetic hysteresis loops of catalysts at room temperature. Reproduced with permission.[66] Copyright 2024, Wiley-VCH. (b) Plots of the reciprocal of magnetic susceptibility ($1/\chi_m$). Reproduced with permission.[67] Copyright 2022, Wiley-VCH. (c) EPR spectra of Fe_{SA}-NSC-90. Reproduced with permission.[68] Copyright 2022, Wiley-VCH. The experimental and simulated cobalt $L_{2,3}$-edge XAS spectra of (d) M-CoPc-RT/400 and (e) B-CoPc-RT/400. Reproduced with permission.[69] Copyright 2023, Nature. (f) *Operando* ^{57}Fe Mössbauer spectra of Fe_1-$NS_{1.3}C$ at different voltage conditions. Reproduced with permission.[70] Copyright 2021, Wiley-VCH. (g) Kβ mainline XES data. Inset of (g): relationship between the relative area of the Kβ′ peak compared to the total Kβ line and the spin state of the reference compounds. (h) *In situ* Kβ mainline; inset: amplification of the Kβ′ area. Reproduced with permission.[71] Copyright 2021, Wiley-VCH.

analysis observed unpaired electrons of Fe single atoms in the catalyst. The *g*-values of 2.005 and 2.026 corresponded to the unpaired electrons in the e_g orbitals of the Fe atoms.

2.2.3. X-ray absorption spectroscopy (XAS). Transitions in the spin state can be identified through XAS at the Co L-edge and O K-edge. The Co L-edge spectrum is split into L_3 and L_2 edges due to spin–orbit coupling, corresponding to transitions from the $2p_{1/2}$ and $2p_{3/2}$ energy levels to the unoccupied 3d orbitals, respectively.[74–77] Additionally, key insights into an electron's symmetry and spin state can be obtained from the contour and adjusted intensity of the Co L_3 side peak. Therefore, the strength of the Co L_3-edge peak serves as a direct indicator of spin behavior.[14] A decrease in the intensity of the phenomenon indicates the conversion from a high-spin (HS) configuration to an intermediate-spin (IS) configuration of Co^{3+}. For example, Liu *et al.* conducted Co L-edge spectroscopy analysis on CoPc and binuclear CoPc supported on carbon with N-doping (NC), named M-CoPc-RT and B-CoPc-RT, to explore the variances in the electronic structure between M-CoPc and B-Co post heat treatment.[69] As shown in Fig. 4d and e, B-CoPc-RT, M-CoPc-RT, and M-Co all had similar Co L-edge XAS spectra, suggesting that the Co in the three samples had a low-spin state ($d_{x^2-y^2}{}^0 d_{z^2}{}^1 d_{xy}{}^2 d_{xz,yz}{}^4$). However, after annealing treatment, the shape of the Co^{2+} L_2-edge and L_3-edge in B-Co changed significantly. The $L_{2,3}$-edges exhibited a shift toward lower binding energies, accompanied by a notable decline in the contribution from 2p to d_{z^2} orbital transitions. This indicated that the ground state of the 3d orbitals had changed due to the different symmetry and ligand field of Co^{2+} in B-Co. Theoretical simulations showed that the electronic ground-state configuration shifted from low spin (b_{1g} ($d_{x^2-y^2}{}^0$), a_{1g} ($d_{z^2}{}^1$), e_g ($d_{xz}{}^2$, $d_{yz}{}^2$), and b_{2g} ($d_{xy}{}^2$)) to high spin ((b_{1g} ($d_{x^2-y^2}{}^1$), e_g ($d_{xz}{}^1$, $d_{yz}{}^1$), a_{1g} ($d_{z^2}{}^2$), and b_{2g} ($d_{xy}{}^2$)).

2.2.4. Mössbauer spectroscopy. Mössbauer spectroscopy, which utilizes Fe^{59} nuclei to observe recoilless γ-ray absorption, is a powerful method for investigating the local coordination structures, oxidation states, and spin polarization configurations of Fe species.[78] In Mössbauer spectroscopy, the identification of Fe ions with varying spin states is possible through analysis of their distinct isomer shift (IS) and quadrupole splitting (QS) values.[79] Both Fe^{2+} and Fe^{3+} exhibit low-spin (LS) states when the IS lower. However, QS is lower in LS Fe^{2+} hybrids and higher in LS Fe^{3+} hybrids compared to their respective high-spin (HS) states.[67] For example, Liu *et al.* identified low-spin

atomic Fe^{3+} atoms in the C–FeN_4–S segment as the active sites of the ORR by *in situ* Mössbauer spectroscopy (Fig. 4f).[70]

2.2.5. Non-resonant X-ray emission spectroscopy (XES). Non-resonant XES is a tool that can be used for quantitative analysis of the average spin states of metal sites, not only to distinguish the oxidation states and spin states, but also for *in situ* experimental acquisition in a few minutes.[71] The Kβ′ satellite peak due to the 3p–3d exchange coupling can be used to analyze the number of unpaired 3d electrons.[80,81] Herran and colleagues investigated the mean spin configurations of two Fe/N/C catalysts using XES, elucidating the electronic makeup of their molecular sites.[71] Fig. 4g presents the XES spectra of both samples, which exhibit a $K\beta_{1,3}$ main line at around 7.058 keV, accompanied by a Kβ′ satellite near 7.044 keV. This satellite arose from 3p–3d exchange interactions, indicating an average spin state >0. The use of a linear fit permitted the relative Kβ′ strength of the Fe/N/C catalysts (see the inset of Fig. 4g) to be interpolated, thereby yielding an average spin state of 0.8 for both samples. Chiefly, the existence of reversible and potentially-induced changes of the spin states in the samples was revealed for the first time by *in situ* X-ray measurements. Fig. 4h shows the XES spectra obtained at OCV and 0.2 V *vs.* RHE, where lowering from OCV/0.9 V to 0.2 V resulted in a mean drop from 0.8 to 0.55, indicating a drop in the mean spin state of the catalyst. However, this change was observed to reverse upon returning to a high potential.

2.3. Regulation of the spin polarization of DACs

The electronic structure of DACs is an important reason for their synergistic effect. Three primary approaches have been devised to regulate the electronic structure of DACs by regulating the spin polarization: regulation of the central atoms, the distance between two metal sites, and the coordination environment.

2.3.1. Regulation of the central atoms. The asymmetric up- and down-spin distribution of 3d transition metals leads to spin polarization, and the spin–spin coupling between the two metals is critical for determining the electronic structure and catalytic properties.[32]

2.3.1.1. Coupled with a homonuclear metal. In homonuclear DACs, two identical metal atoms are situated adjacent to one another and may form a bond.[1] Huang *et al.* developed a NPs-to-SAs-to-DAs atomization and sintering method *via* a N-removal and heat-induced migration process (Fig. 5a).[82] To be specific, it was shown that it was possible to adjust the existing configurations of Co species at the atomic scale, thereby producing nanoparticles, CoN_4 SAs, and Co_2N_5 DAs on hollow carbon spheres with N-doping. The difference in Gibbs free energy between ΔG_{OOH^*} and ΔG_{OH^*} ($|\Delta G_{OOH^*-OH^*}|$) is a significant descriptor for the ORR/OER, and ideally should be valued at 2.46 eV. As shown in Fig. 5b, the spin magnetic moment exhibited a positive, nearly linear correlation ($R^2 = 0.962$) with $|\Delta G_{OOH^*-OH^*}|$. The Co_2N_5 dual atom's ΔG_{OOH^*} to ΔG_{OH^*} coordinate was near the ideal scaling relation with a $|\Delta G_{OOH^*-OH^*}|$ value of 2.55 eV, near to the ideal 2.46 eV for ORR/OER catalysts (Fig. 5c). This suggests that Co_2N_5 has the most suitable O* intermediate adsorption/desorption energy. The likely reason for this is that the reduced spin magnetic moment of Co_2N_5 disrupts the universal ΔG_{OOH^*} to ΔG_{OH^*} scaling relation, leading to an optimal balance of O* adsorption.

2.3.1.2. Coupled with a heteronuclear metal. In heteronuclear DACs, two distinct metal atoms are positioned next to each other, potentially forming a bond.[1] Zhao *et al.* employed DFT to forecast that Fe–Ni dual-atom active centers would demonstrate moderate spin magnetization at the reaction sites and possess limited spin-polarized conduction electrons.[33] Fe 3d, the active center of Fe–N–C, exhibits high spin polarization, with a spin magnetic moment value of 1.88 μ_B, and localized charge distribution. However, the metal of Ni–N–C is paramagnetic, and the spin magnetic moment value is almost zero. By constructing a heteronuclear Fe–Ni dual-atom pair, the spin coupling between the two metals weakened the spin polarization of the Fe 3d electron and reduced its spin magnetic moment to 1.48 μ_B (Fig. 5d and e). Based on the theoretical research results, an Fe/Ni–N–C catalyst with bifunctional ORR/OER performance was prepared by a wet chemical approach.

2.3.2. Adjustment of the distance between two metal sites. The close distance between two neighboring metal atoms could induce a heavy electronic interaction, regulating the spin state of the metal atom and the d-band center; hence optimizing the adsorption and desorption of reactant molecules or intermediates to promote the catalytic activity.[83] Luo *et al.* synergistically modulated the electronic characters and catalytic performances of Fe active sites in $FeMn_6$-DACs and $FeMn_8$-DACs by utilizing the non-covalent interactions of the dual metals (M = Fe, Co, Ni, Cu, and Zn).[60] Specifically, when the Fe–M distance was less than 15 Å (Fig. 6a), the non-bonding interaction was remarkable. The minimal overpotentials for the ORR (denoted as η_{ORR}) for $FeNiN_6$-DACs and $FeNiN_8$-DACs were predicted by DFT calculations, and were due to the high Bader charge transfer and high spin density at Fe sites in the $FeNiN_6$-DAC and $FeNiN_8$-DAC systems (Fig. 6b), promoting the desorption of H_2O molecules.

Zhang *et al.* successfully synthesized Mn–Fe binuclear sites, anchored on a GO-like structure.[86] The findings from aberration-corrected high-angle annular dark-field scanning transmission electron microscopy (AC-HAADF-STEM) analysis revealed an approximate distance of 0.3–0.4 nm between the Mn and Fe atoms. This distance was consistent with the approximate sum of their van der Waals radii, and the proximity of two atomic sites may result in a small-distance electronic interaction. The small-distance electronic interaction between the Mn and Fe atom sites resulted in a transformation of the Fe spin state from a medium to a high-spin state. According to Sabatier's principle, the d_{z^2} orbital of Fe in the high self-selection state is half-full, which is conducive to the absorption and desorption of oxygenated species during the ORR.

2.3.3. Designing the coordination environment. Designing the local coordination environment is a highly efficient technique for regulating the spin states of DACs. The introduction of nonmetal atoms, such as N, S, O, and P, into DACs can improve the electrocatalytic activity, because they can provide an electron absorption/supply environment, share lone pairs of

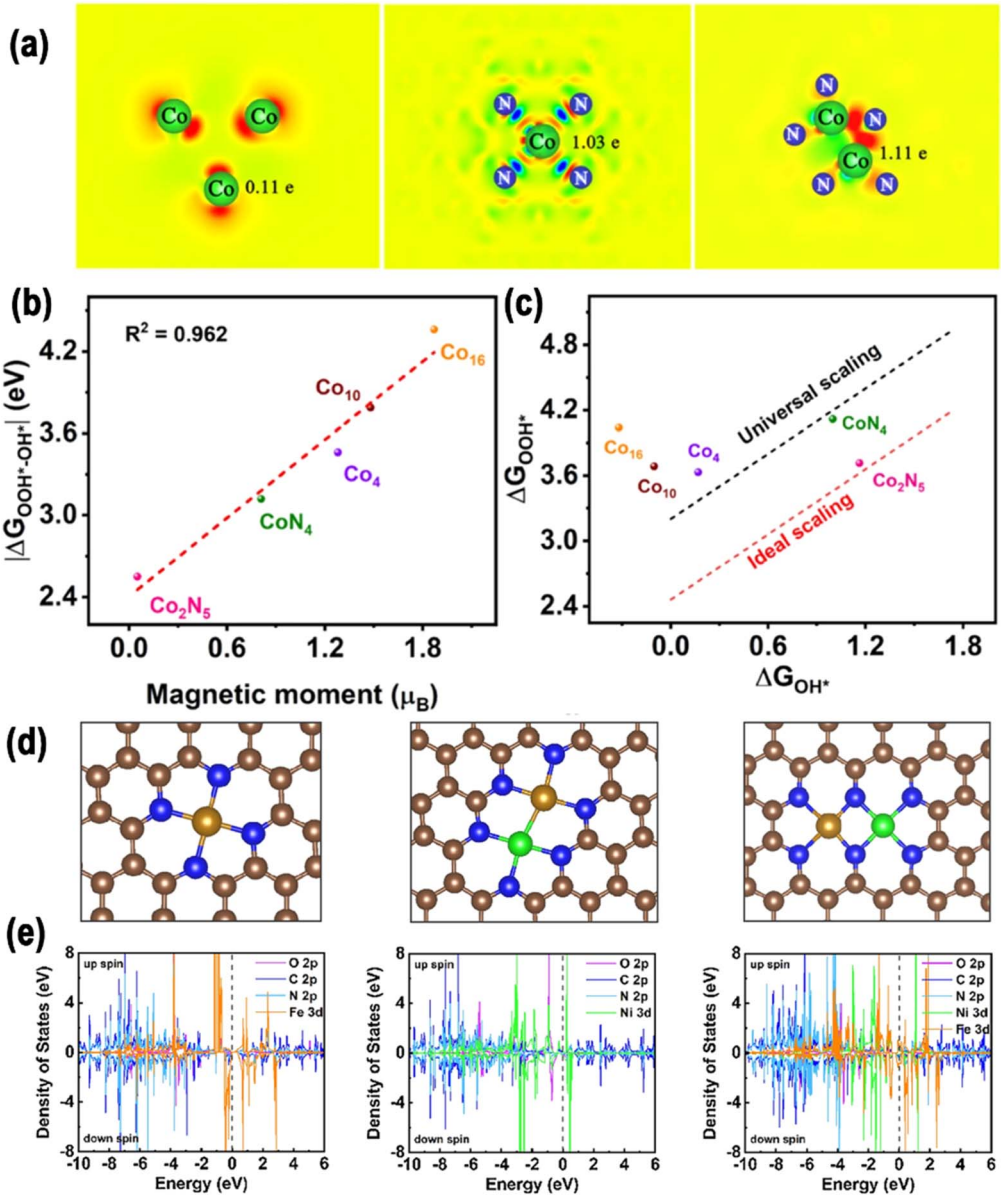

Fig. 5 (a) Bader charge diagrams; (b) direct relationship between the magnetic moment and $|\Delta G_{OOH^*-OH^*}|$. (c) Comparison of the scaling of ΔG_{OOH^*} to ΔG_{OH^*} for all models to the universal and ideal scaling lines[82] Copyright 2022, Nature. (d) Diagrammatic representation of M–N–C (where M = Fe or Ni), Fe/Ni–N–C (coordinated with 3 N atoms), and Fe/Ni–N–C (coordinated with 4 N atoms, with 2 N atoms shared by Ni and Fe). (e) Density of states for all the samples. Reproduced with permission.[33] Copyright 2021, Elsevier.

electrons, and achieve an accurate modulation of electronic structures.[87–90] To investigate the impact of various N-coordinated configurations on the excellent performance of DACs, Zhao *et al.* analyzed the electronic structure of two FeFeNC structures *via* DFT calculations.[84] As shown in Fig. 6c and d, the spin-related channel around the Fe sites in FeFeNC-3 was significantly broader than that in FeFeNC-4, demonstrating that the Fe site in FeFeNC-3 was more likely to adsorb O-related intermediates. Moreover, since the magnetic moments between the Fe atom pairs in the two catalysts were the same, both of them tended to adsorb O_2 in a horizontal adsorption configuration, which facilitated O=O dissociation and thus promoted the ORR kinetics. In addition, due to the variation of TMs in DACs on the left of the element periodic table, the dual-metal active sites demonstrated a higher spin polarization, giving rise to a more robust adsorption of *OH and a reduction in ORR activity.

Liu *et al.* proposed an S-doped di-nuclear Fe-based ORR catalyst (Fe_2N_6-S) by simulating the catalytic center of ferredoxin, which was composed of Fe–Fe dual-metal sites and nonmetal S sites.[85] In this process, the second Fe site and the heteroatom S act as "double modulators" in conjunction with one another to complete the accurate tuning of the electronic configuration. Additionally, spin-polarized DFT was predominantly utilized to anticipate the impact of the Fe–NC coordination structure on the O_2 absorption characteristics. This is

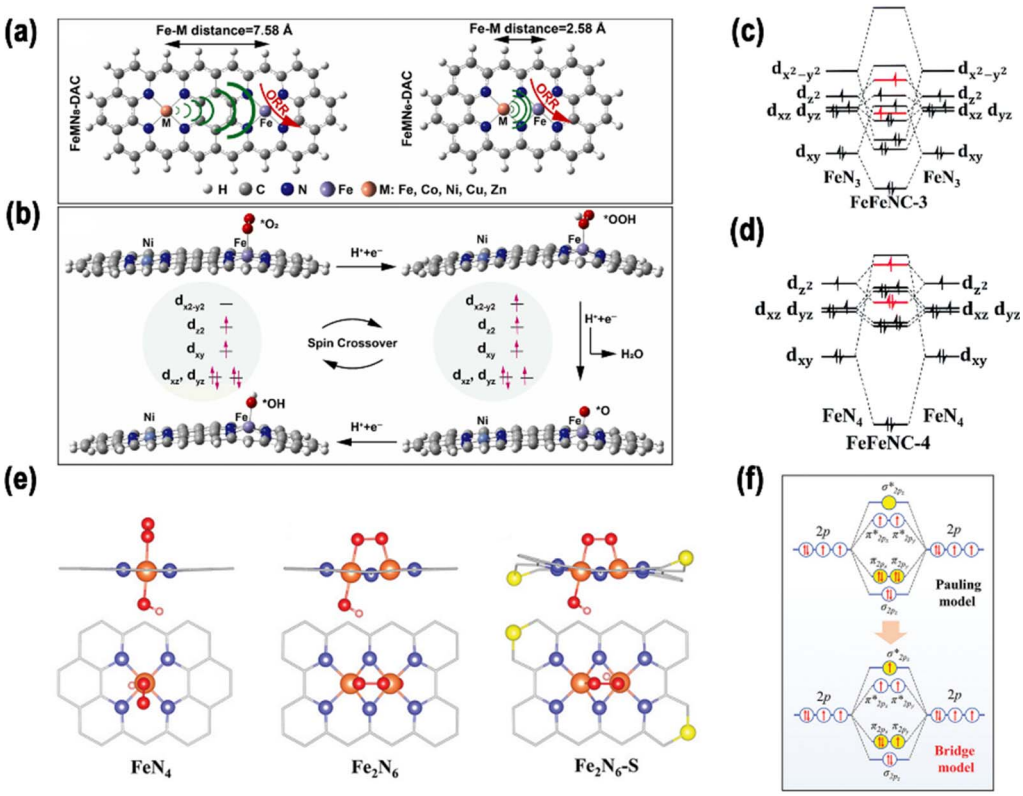

Fig. 6 (a) Structures of $FeMN_6$-DAC and $FeMN_8$-DAC. (b) Side perspective of reaction intermediates of $FeNiN_8$-DAC in the ORR. Reproduced with permission.[60] Copyright 2023, Elsevier. Orbital interactions between Fe atoms in (c) FeFeNC-3 and (d) FeFeNC-4. Reproduced with permission.[84] Copyright 2022, the Royal Society of Chemistry (e) geometric models of FeN_4, Fe_2N_6, and Fe_2N_6-S with absorbed O_2. (f) Schematic representation of the potential electron orbital configurations of O 2p orbitals in various oxygen-adsorption arrangements. Reproduced with permission.[85] Copyright 2023, Wiley-VCH.

a critical determinant of the ORR activity. First, three kinds of carbon-based electrocatalyst models were constructed, as shown in Fig. 6e, in which four N atoms cooperated with Fe SA, Fe DA, and S-doped Fe DA, which were defined as FeN_4, Fe_2N_6, and Fe_2N_6-S, respectively. Second, in a follow-up study, the authors modified the structures of FeN_4, Fe_2N_6, and Fe_2N_6-S with OH*. The migration of electrons from the bonding orbital π_{2px} or π_{2py} to the antibonding orbital π^*_{2pz} in the bridge model weakened the O–O bond, thereby promoting the subsequent reaction process (Fig. 6f). These initial theoretical findings indicate that the dual Fe–Fe sites play a pivotal role in optimizing the oxygen-adsorption behavior, facilitating the efficient activation of O–O bonds, and consequently, enabling the acceleration of the ORR kinetics. Furthermore, the doping of S atoms around the Fe–Fe sites also exerts a modulating influence on the oxygen binding energy.

3. Spin effect in dual-atom electrocatalysis

Recently, it has been increasingly acknowledged that the spin state of DACs plays a pivotal role in determining their catalytic activities for the HER,[91] CO_2RR,[92] NRR,[93] ORR,[94] and OER.[20] Modulation of the spin states offers the possibility to accurately design DACs with optimized electronic structures and good performances. In the following, we introduce the application of the spin-state regulation of DACs in various catalytic reactions in detail.

3.1. Oxygen electrocatalysis

Clean and renewable energy sources and energy-conversion techniques have attracted extensive interest due to the current global energy and environmental challenges, and include metal–air batteries, fuel cells, and electrochemical water decomposition. Oxygen electrocatalytic reactions play a key role in these applications, determining the efficiency of hydrogen/oxygen-related reactions. Oxygen electrocatalytic reactions include the OER and ORR. From the perspective of orbital mechanics, oxygen molecules exist in two distinct spin states, the triplet state ($^3O_2$, ground state), which is the lowest energy configuration and represents the ground state, and the singlet state ($^1O_2$, metastable state), which is a metastable state.[95] $^3O_2$ is generally considered to be the dominant form of oxygen in electrocatalysis due to its energy (0.00 eV) being lower than that of $^1O_2$ (0.98 eV).[95] As shown in Fig. 7, since the spin quantum number of oxygen species is not conserved between the OER and ORR, the high energy barrier of the two reactions is associated with spin-state transitions involving spin electrons, such

as the singlet OH^-/H_2O to $^3O_2$ spin transition.[25] Therefore, DACs have been developed to reduce energy expenditure by reducing the energy barrier and promoting spin transitions.[96]

3.1.1. Oxygen reduction reaction

3.1.1.1. ORR mechanisms. As shown in Fig. 8, the ORR typically follows two reaction pathways on DACs: the reduction of O_2 through OOH*, O*, and OH* intermediates, resulting in the formation of two H_2O molecules *via* a $4e^-$ pathway, or the formation of an H_2O_2 molecule *via* a $2e^-$ transfer pathway. Depending on the reaction pathway, it can be further divided into the dissociation mechanism (DM) and the association mechanism (AM).[97,98] The $4e^-$ transfer of $^3O_2$ and $^1O_2$ in the DM (right of Fig. 8b) was taken as an illustration by Chen *et al.* to demonstrate the electron-transfer mechanism of the ORR.[95] In the case of the $^3O_2$RR, the π^* orbital of $^3O_2$ contains two unpaired electrons with parallel spins, requiring the first and second transferred electrons to have antiparallel spins to those already present. In accordance with the supposition that the electrons in the π^* orbitals of $^3O_2$ are in an up-spin configuration, the subsequent electrons should accordingly be in a down-spin configuration. Following the acceptance of these electrons by the two π^* orbitals of the adsorbed O–O intermediate, the third electron is constrained to occupy only the higher-energy σ^* orbital of the adsorbed OOH intermediate due to orbital occupancy constraints. The higher-energy antibonding orbital, which is filled by electrons, results in an instability of the O–O bond. This instability causes the adsorbed OOH to transform into adsorbed O and OH^- intermediates. It could be postulated that the third electron occupies an orbital of the adsorbed O intermediate, with its spin likely antiparallel to the unpaired t_{2g} electron. Finally, the last spin-down electron pairs with the third electron. For $^1O_2$RR, the presence of an empty π^* orbital indicates that the initial electron transfer is not impeded by Coulomb repulsion. It is highly likely that the spin orientation of the initial electron is opposite to that of the unpaired t_{2g} electron. Subsequent electron transfers from the second to the last electron follow the same steps as in $^3O_2$RR.

3.1.1.2. Spin effect in the ORR. Due to their maximum atomic utilization, adjustable electronic structures, and tunable coordination environment, SACs exhibit extraordinary activity and selectivity in the ORR.[99,100] Despite the achievement and progress made by SACs, one of the most significant challenges in the exploitation of SACs is the scaling relationship between the adsorption/desorption toward a complicated multi-intermediate limit.[101] Fe–N_4 single-atom sites, characterized by a clearly defined structure, demonstrate a robust interaction with O species. This interaction presents a challenge during the ORR process, as it hinders the conversion of *O to *OH through protonation.[102] In a study by Chen *et al.*, an approach was taken to optimize the binding energy of O species.[103] To this end, they constructed a catalyst featuring diatomic sites with FeCo molecular heterostructures. The FeCo-MHs were formed by overlapping CoPc molecules on FePc molecules, with the degree of overlapping dependent on the level of partial or complete overlap (Fig. 9a and b). As shown in Fig. 9c, the formation of the FePc/CoPc molecular heterostructure endowed the catalyst with higher performance in ORR/OER processes. In contrast to its Fe–N_4 single-atom site counterpart, the heterostructure comprising molecular components was observed to influence the magnetic moments of the metal active centers, thereby increasing the proportion of the low-spin Fe(II)–N_4 unit, which exhibited higher intrinsic activity compared to the intermediate-spin form. This optimized the intrinsic activity of the ORR ($E_{1/2} = 0.95$ V) at the summit of the volcano plot (Fig. 9d and e). It is worth noting that the arrangement of the FeCo molecular heterostructure could regulate the magnetic moments of both the Fe center (from 1.97 to 2.01) and the Co center (from 1.03 to 0.98) and thus change the binding strength for *O (Gibbs free energy from 4.95 to 1.42 eV), *OH (2.91 to 0.90 eV), and *OOH (5.35 to 4.06 eV) (Fig. 9f–h), which confirmed that the spin effect, achieved by building molecular heterostructures with dual-atom sites, is an effective strategy for regulating the ORR/OER catalytic activity.

Additionally, during the extended ORR process, the intermediate valence state of Fe^{2+} can initiate various side reactions, resulting in a degradation of the performance of Fe-based SACs. Li *et al.* reported a distinct electronic structure with half-metallic characteristics in a diatomic Fe/Zn–N–C catalyst,

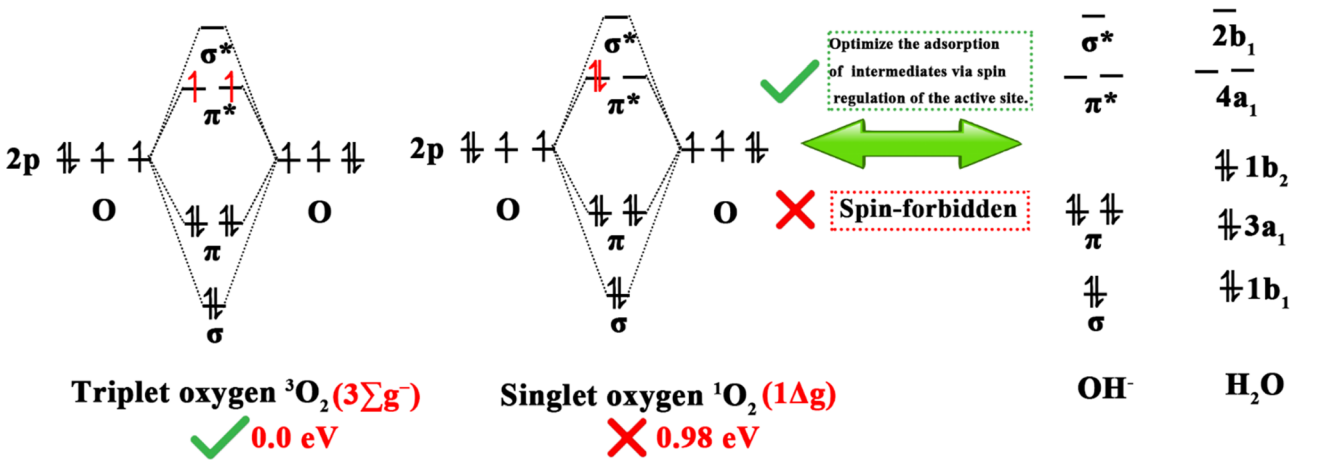

Fig. 7 Electronic configurations of singlet OH^-, H_2O, $^1O_2$ and $^3O_2$.

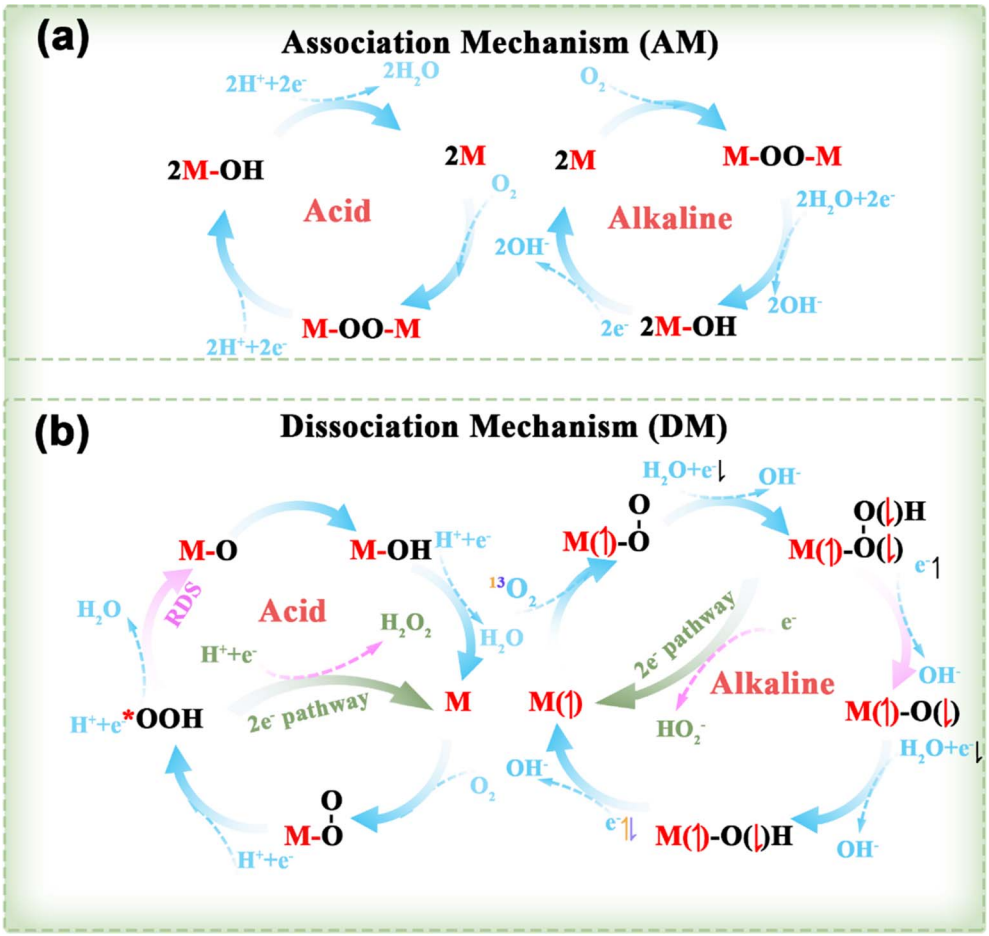

Fig. 8 Several reaction pathways for the ORR involving an (a) AM and (b) DM in both acidic and alkaline environments, alongside the mechanisms of the $^3O_2$RR and $^1O_2$RR, taking into account the spin of the transferred electrons.[97,98]

induced by the cooperative effects of Fe and Zn, as revealed through theoretical screening.[104] This unique structure could generate spontaneous spin-polarized conduction electrons near the Fermi level (E_F), thereby improving the capture and bonding of O_2 molecules. Specifically, a conversion from a semiconductor to half-metal was noticed in the catalyst with the coordination of Zn (Fig. 9i and j), resulting in the emergence of spontaneous spin-polarized electrons at the E_F. As explained above, in the stray field of a spin-polarized catalyst, the spins of two unpaired electrons in the antibonding π^* orbits of paramagnetic O_2 align in the same direction.

The full spin polarization of itinerant electrons promotes the formation of a bonded state, improving the capture of O_2, which is the initial step in the ORR process. Binding energy calculations indicated that the adsorption of $*O_2$ enhances the activity in Fe/Zn–N–C. On the other hand, DACs demonstrate greater stability during protonation. The protonation diagrams (Fig. 9k and l) showed a theoretical overpotential of 0.41 V for Fe/Zn–N–C after 2*H adsorption, matching the pre-protonation value, which confirmed that DACs could maintain their reactivity after post-protonation. This occurs because the protonation process leaves the electronic structure of the FeN_4 active center unchanged (though ZnN_4 is altered to ZnN_2). As a result, the fully spin-polarized conduction electrons at the E_F are preserved, maintaining the DACs' high reaction activity. Additionally, after protonation, the bond lengths of Fe–N_3 and Fe–N_4 were slightly increase from 1.79 to 1.91 Å (Fig. 9m). This change helps protect the FeN_4 sites, ensuring a continuous and durable ORR process. The synthesized Fe/Zn–N–C showed exceptional ORR activity, with $E_{1/2}$ values of 0.91 V in 0.1 M KOH and 0.81 V in 0.1 M $HClO_4$, significantly surpassing those of Fe–N–C and Zn–N–C.

3.1.2. Oxygen evolution reaction

3.1.2.1. OER principles. Based on the established AEM and LOM routes, a potential mechanism for the generation of $^3O_2$ and $^1O_2$ was suggested by taking into account the spin orientation of the $4e^-$ transfer during the OER (Fig. 10).[95] LOM occurs when the oxygen p-band of lattice oxygen is elevated above the metal d-band center. O_2 molecules produced *via* the LOM pathway originate from two sources (Fig. 10a): either both oxygen atoms originate from the oxide lattice, or one comes from the lattice oxygen while the other is sourced from the electrolyte (right in Fig. 10a). The AEM pathway includes two subcategories: Eley–Rideal (ER) (left in Fig. 10b) and Langmuir–Hinshelwood (LH) (right in Fig. 10b).

3.1.2.2. Spin effect in the OER. The OER is essential for devices involved in energy-related fields, such as water splitting, fuel cells, and metal–air batteries (MABs).[105–107] Basically, the

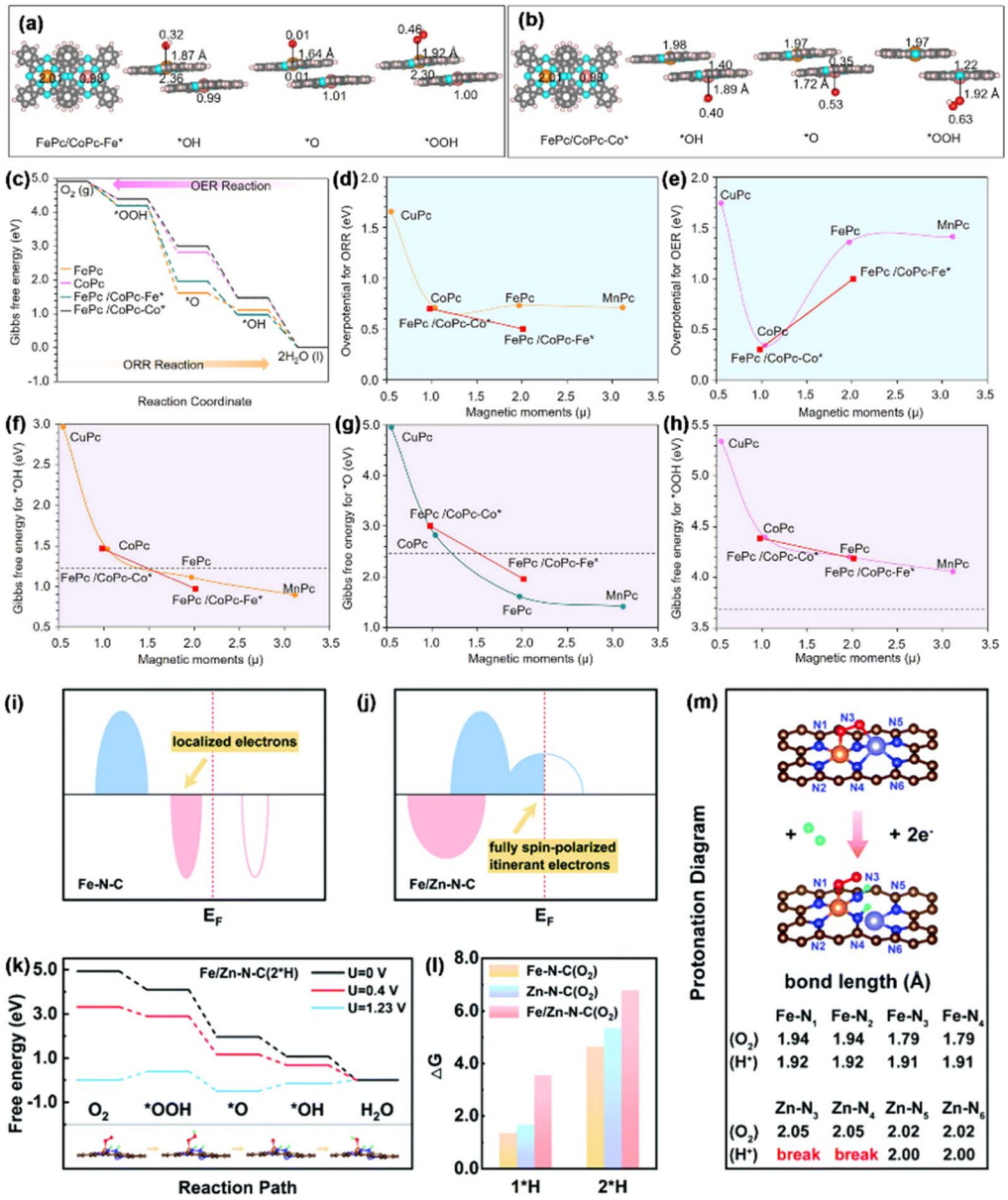

Fig. 9 Optimized configurations of (a) FePc/CoPc-Fe* and (b) FePc/CoPc-Co* together with their respective intermediates. (c) Gibbs free energies for the ORR/OER. Graphs depicting overpotential *versus* magnetic moment (μ) for (d) the ORR and (e) OER. Magnetic moment analysis together with (f) *OH, (g) *O, and (h) *OOH. Reproduced with permission.[103] Copyright 2023, American Chemical Society. (i and j) Diagrammatic representations of the electronic configurations of Fe–N–C and Fe/Zn–N–C. (k) Free energy of Fe/Zn–N–C. (l) ΔG_{1^*H} and ΔG_{2^*H} for catalysts exposed to O_2. (m) Protonation map of Fe/Zn–N–C. Reproduced with permission.[104] Copyright 2022, the Royal Society of Chemistry.

OER process is thermodynamically challenging, involving multiple steps of proton-coupled electron transfer, and the inherently slow reaction dynamics requires highly efficient catalysts to lower the reaction overpotential for practical use.[108] At present, many DACs have been effectively synthesized and implemented in applications pertaining to the OER.[109–113] Nevertheless, the spin reaction mechanism at dual-metal active sites for improving the OER activity still needs further investigation.

Patzke *et al.* synthesized Ni, Co, and Fe single-atom sites, as well as Ni–Fe dual-atom sites on g-C_3N_4, denoted as Ni-CNG, Co-CNG, Fe-CNG, and NiFe-CNG.[114] To gain insights into the adsorption behavior at Fe and Ni sites, they employed DFT calculations to assess the spin density of the catalysts. In all the samples (Fig. 11a–c), the results showed that Ni atoms exhibited a low-spin configuration, whereas Fe atoms demonstrated a high-spin configuration, revealing the presence of unpaired electrons in both the t_{2g} and e_g orbitals of Fe. In the *in situ*-formed Ni–O–Fe bonds, spin disparities between the Ni and Fe sites enhanced electron transfer during the OER process by establishing effective spin channels. Meanwhile, a new OER mechanism involving cooperative interaction between Ni and Fe sites in dual-site NiFe DACs was proposed (Fig. 11d). The OER initiation hinged on intricate interatomic electronic

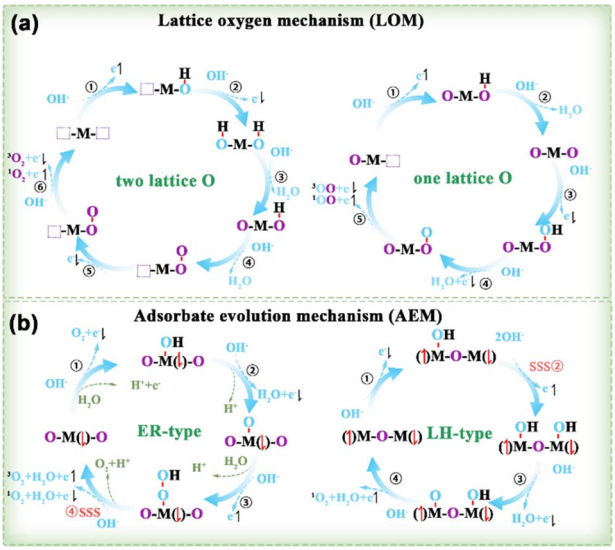

Fig. 10 (a) LOM and (b) AEM of OER examined by taking into account the spin of the transferred electrons.[95] M denotes the metal site, with the adjacent arrow indicating the spin direction of unpaired t_{2g} electrons. Purple O and blue O represent the lattice and adsorbed O species, respectively. SSS stands for the spin selective step.

interactions at emerging Ni–O–Fe active sites. The local electronic structure was optimized to take advantage of unobstructed spin channels within the Ni–O–Fe bonds, thereby significantly augmenting the adsorption energies of the intermediates.

Lu *et al.* reported a Mg–Fe dual-site catalyst (denoted as $MgFeN_5C$) immobilized on a nitrogen-doped carbon substrate for the OER fabricated by an easy wet chemical method.[115] The study found that introducing the Mg element into the Fe–N–C structure causes a significant mismatch in the ionic radii of Mg^{2+} and Fe^{2+} ($r_{Mg^{2+}}$ = 7.2 Å, $r_{Fe^{2+}}$ = 6.1 Å). This mismatch induces local crystal-field distortion in the FeN_4 plane, elevating the energy level of Fe d_{z^2}. Consequently, Fe^{2+} undergoes a spin transition from an intermediate state ($d_{xy}^2 d_{xz}^2 d_{yz}^1 d_{z^2}^1$, 2.96 μ_B) to a low state ($d_{xy}^2 d_{xz}^2 d_{yz}^2$, 0.95 μ_B). The low-spin (LS) state, characterized by smaller bond order, alleviates the effect of ΔG_{*O}. As shown in Fig. 11e, in a typical FeN_4 site, the central metal and circumambient N atoms exhibited an in-plane D_{4h} symmetry, splitting the fivefold degenerate orbitals into d_{xy}, d_{z^2}, d_{xz}/d_{yz}, and $d_{x^2-y^2}$. Fe^{2+} attained the intermediate spin (IS) state through the partially occupied spin-up and spin-down channels. A strong interaction between Fe^{2+} and O intermediates arose from the unpaired d_{z^2} and $d_{xy/yz}$ electrons, causing a maximal overlap of *O/*OH and *OOH with $O2_{pz}/2_{py}$ and π* along the *z*-direction (Fig. 10f and g). However, in the dual-site Mg/Fe, the significant difference in ionic radii from Mg to Fe led to geometric distortion in the FeN_4 moiety. DFT calculations revealed that within the $MgFeN_5C_1$ moiety, the three lowest orbitals—comprising $d_{x^2-y^2}$ and the degenerate $d_{xz/yz}$—were completely took up in the spin-up and spin-down channels. Conversely, the d_{z^2} orbital was vacant, resulting in a low-spin (LS) state and consequently a reduced bond order with *O. To experimentally confirm the spin repartition, the authors conducted temperature-dependent magnetic susceptibility (χ_m) studies under ZFC-T conditions and employed EPR spectroscopy analysis. These analyses elucidated the electron spin allocations. The μ_{eff} values of Fe–N–C and Mg/Fe–N–C were calculated to be 2.96 μ_B and 0.95 μ_B, respectively (Fig. 10h and i). The d-electron count of Fe^{2+} declined from around 2.12 in Fe–N–C to about 0.38 in Mg/Fe–N–C, significantly affecting the geometry of the signal peaks (Fig. 11j), as acknowledged in the field for its impact on electron–environment interactions. Therefore, these results indicate that local field distortion can effectively adjust Fe spin configurations, and the LS state is more favorable for enhancing the intrinsic OER performance.

Recent studies have indicated that the high electronegativity of the coordinated N hinders intermediate adsorption at the metal center, raising the potential barrier and reducing the reaction kinetics.[116] Therefore, Hu *et al.* utilized a P-doped metal—organic framework as a porous substrate to synthesize Co_1-PNC/Ni_1-PNC, with a P atom replacing a N atom in the M–N_4 structure. This modification enhanced the electron spin density and altered the electronegativity, resulting in improved ORR/OER activities.[117] The catalyst demonstrated high OER activity with η_{10} = 0.39 V, outperforming Co_1–NC/Ni_1–NC (η_{10} = 0.41 V) synthesized without P-doping.

3.2. Hydrogen evolution reaction

3.2.1. HER principles. In the electrochemical process of water splitting, the HER serves as the cathodic half-reaction. This reaction encompasses a two-step reduction mechanism. The initial step of the reaction sequence is the Volmer reaction. This is subsequently followed by either the Tafel process or the Heyrovsky process, depending on the specific reaction pathway. In strong acidic solutions, hydronium ions (H_3O^+) are the source of protons for the HER.[118] In Step (1) (Volmer step), in an acidic electrolyte, an H_3O^+ ion adsorbs onto the surface, where it combines with a surface electron to form an adsorbed H*.[118,119]

$$H^+(aq.) + e^- \rightarrow H_{ads} \quad (1)$$

Step (2) can proceed *via* two distinct pathways: when the surface concentration of H* is high, two H* species combine to form H_2 in a process known as the Tafel step, which involves chemical desorption.

$$H_{ads} + H_{ads} \rightarrow H_2(g)$$

Otherwise, H* reacts with another $H_3O^+ + e^-$ (*via* proton-coupled electron transfer) to form H_2 (Heyrovsky step, electrochemical desorption).

$$H_{ads} + H^+(aq.) + e^- \rightarrow H_2(g)$$

This process is shown in Fig. 12a. Similarly, in alkaline electrolytes, the HER mechanism follows either the Volmer–

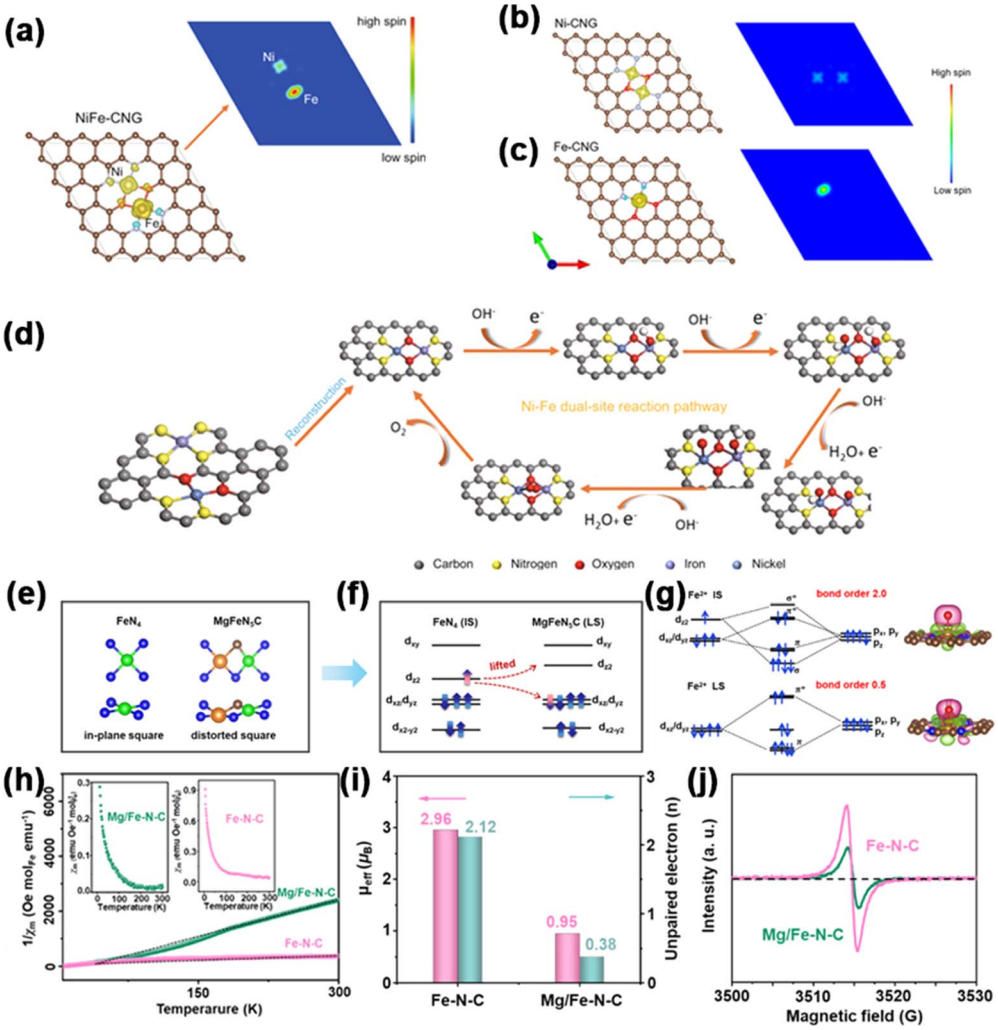

Fig. 11 Spin density schema and spin channels of (a) NiFe-CNG, (b) Ni-CNG, and (c) Fe-CNG. (d) Proposed OER pathway diagram. Reproduced with permission.[114] Copyright 2021, Nature. (e) Local geometry. (f) Spin state. (g) Charge density difference. (h) $1/\chi_m - T$ curves; inset of (h) shows $\chi_m - T$ curves. (i) μ_{eff} and number of unpaired electrons (n) for Fe–N–C and Mg/Fe–N–C. (j) EPR spectra. Reproduced with permission.[115] Copyright 2023, Wiley-VCH.

Tafel or Volmer–Heyrovsky pathway, with water molecules acting as the reactant (Fig. 12b).

3.2.2. Spin effect in the HER. Alkaline water electrolysis is a green and environmentally friendly method for hydrogen production on a large scale.[120] At present, Pt/C is still recognized as the most highly efficient HER electrocatalyst. Designing atomic catalysts that mimic or surpass Pt-like HER performance remains highly desirable.[121] Owing to the synergistic effect of the two metal atoms in DACs, the adsorption/desorption energy barrier of the H* or OH* intermediates is set close to zero and hydrogen evolution is enhanced.[90]

Huang and colleagues developed a strategy for the atomization and sintering of nanoparticles, single atoms, and diatoms (NP–SA–DA).[82] This approach allowed generating Co nanoparticles, CoN_4 single atoms, and Co_2N_5 diatoms on N-doped hollow carbon spheres. In the HER, the spin magnetic moment is negatively linearly related to the Gibbs free energy of H* (ΔG_{H^*}). Further, ΔG_{H^*} decreases linearly with the increase in the spin magnetic moment. Additionally, the dual-atom Co_2N_5 exhibited the highest ΔG_{H^*}, suggesting that incorporating homonuclear Co atoms results in a low-spin state. This low-spin state is beneficial for the balanced adsorption and desorption of H* intermediates, thereby enhancing the HER performance. The Gibbs free energy of H* intermediates for HER in Co_2N_5 and CoN_4 revealed that the Co_2N_5 dual-atom configuration had an H* adsorption energy of −0.04 eV. This value is nearer to 0 eV, signifying superior HER activity.

3.3. Electrocatalytic carbon dioxide reduction reaction

3.3.1. ECO_2RR principles. The ECO_2RR proceeds *via* a multi-proton-electron coupling process under different catalysts and conditions, following pathways involving $2e^-$, $4e^-$, $6e^-$, $8e^-$, $12e^-$, or higher electron numbers, and each reaction pathway leads to different reduction products.[122] As shown in Fig. 13, the products could be mainly classified as C_1, C_2, and C_3 products, such as CO, HCOOH, or $HCOO^-$, $H_2C_2O_4$ or $C_2O_4^{2-}$, CH_4, HCHO, CH_3OH, C_2H_4, and CH_3CH_2OH.[124]

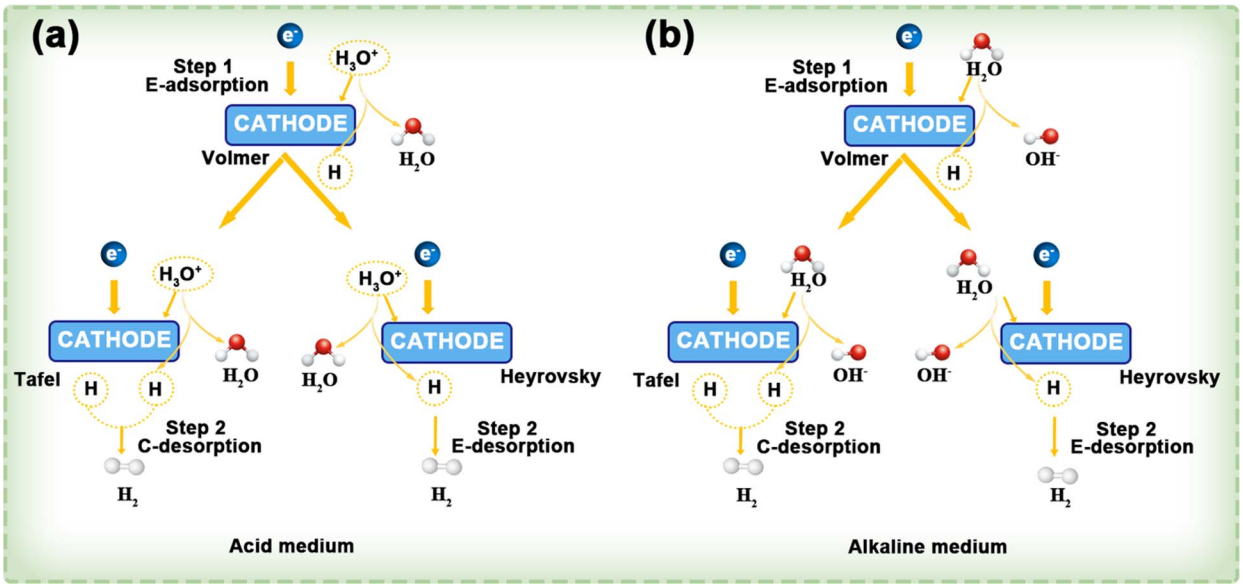

Fig. 12 In both acidic (a) and alkaline (b) environments, the HER follows the Volmer–Tafel and Volmer–Heyrovsky mechanisms. The terms E- and C- indicate electrochemical and chemical processes, respectively. Reproduced with permission.[119] Copyright 2022, American Chemical Society.

3.3.2. Spin effect in the ECO_2RR. As part of the carbon-neutral energy cycle, the ECO_2RR is crucial in addressing the challenges of global climate change and the ever-growing energy demands. The ECO_2RR not only contributes to environmental goals by reducing carbon emissions, but also enables the storage of excess renewable electricity as chemical energy in fuels.[125,126] SCAs are challenging for the ECO_2RR due to their complex intermediates and unmatched electronic structures, as each catalyst typically offers only a single metal active site for adsorption.[127] On the other hand, DACs can provide both top and bridge adsorption sites, thereby facilitating the adsorption of complex intermediates.[128] The electron spin state of metals plays a crucial role in adsorption, reactant and intermediate production, and electron transfer, thereby regulating the selectivity and barrier for C–C coupling in the ECO_2RR.[129]

In work by Lu and co-workers, FeCo–NC and Fe–NC/Co–NC were adopted as probes to investigate the ECO_2RR performance, aiming at the potential formation of C_1 product.[127] First, the models were decided on using spin-polarized DFT (Fig. 14a). It was shown that dual atoms of Fe and Co collaborate to provide bridge sites for stable CO_2 adsorption and modify the electronic structure by analyzing CO_2 adsorption configurations and energy (Fig. 14b–d). Also, electronic DOS analysis revealed the impact of the $\eta^{Fe}(C)$–$\eta^{Co}(O)$ configuration on FeCo–NC (Fig. 14e and f). These give FeCo–NC a significant advantage in CO_2 adsorption and initial activation compared to the corresponding SACs. The energy levels of the Fe and Co diatomic center d-orbitals in FeCo–NC were found to align closely with the CO $2\pi^*$ orbitals around −1.00 eV, as revealed by the DOS analysis of CO adsorption. The interplay between these orbitals leads to the constitution of a partly filled d–$2\pi^*$ orbital below the E_F and an empty d–$2\pi^*$ orbital above it, which is essential for the stable adsorption of CO. Due to powerful spin polarization, the majority α-spin orbitals receive considerable exchange stabilization energy. The α-spin d-orbitals at the Fe and Co dual-atom centers exhibited an energy level of 2.00 eV, which is lower than the energy level of the CO $2\pi^*$ orbitals. Additionally, the spin density diagram (Fig. 14g) showed there was significant spin polarization at the Fe and Co diatomic centers, facilitating CO adsorption and activation.

The μ_{eff} value can reveal the influence of different spin states on C–C coupling. For instance, through spin-polarized DFT, Liu's group showed that M@X-C_2N (M = Fe, Co, Ni, and Cu; X = B) exhibited stronger functionality than single/double-M centers in promoting the CO_2RR, with a particular enhancement observed in C–C coupling.[130] Specifically, the energetics and spin moment of C–C coupling *via* from *COCHO to *CO–CHO, from *COCOH to *CO–COH, and from *COCO to *CO–CO were calculated, as displayed in Fig. 14h. As depicted in Fig. 14i–k, among M@B-C_2N (M = Fe ($\mu = 2\ \mu_B$), Co ($\mu = 1\ \mu_B$), and Ni ($\mu = 0\ \mu_B$)), Fe@B-C_2N showed the lowest Gibbs free energy barrier of 0.17 eV. Among them, Ni@B-C_2N ($\mu = 0\ \mu_B$) primarily produces CH_4, exhibiting the lowest energy barrier at 0.42 eV. On Fe–B or Co–B sites, the transition from *COCHO to *CO–CHO ($\Delta\mu = 2\ \mu_B$) was more favorable than the transition from *COCOH to *CO–COH. On Ni–B sites, both transitions—*COCHO to *CO–CHO and *COCOH to *CO–COH were equally probable with $\Delta\mu = 0\ \mu_B$. This indicates that C–C coupling feasibility depends on the initial spin state and intermediates. Fig. 14l illustrates that the high-spin state of the M–B dual-atom sites significantly enhances the energetics of both chemical and electrochemical coupling processes. Specifically, chemical C–C coupling (*COCO → *CO–CO) and the electrochemical coupling (*COCO + H^+ + e^- → *COCHO) are more actively beneficial under these conditions, indicating that the high spin

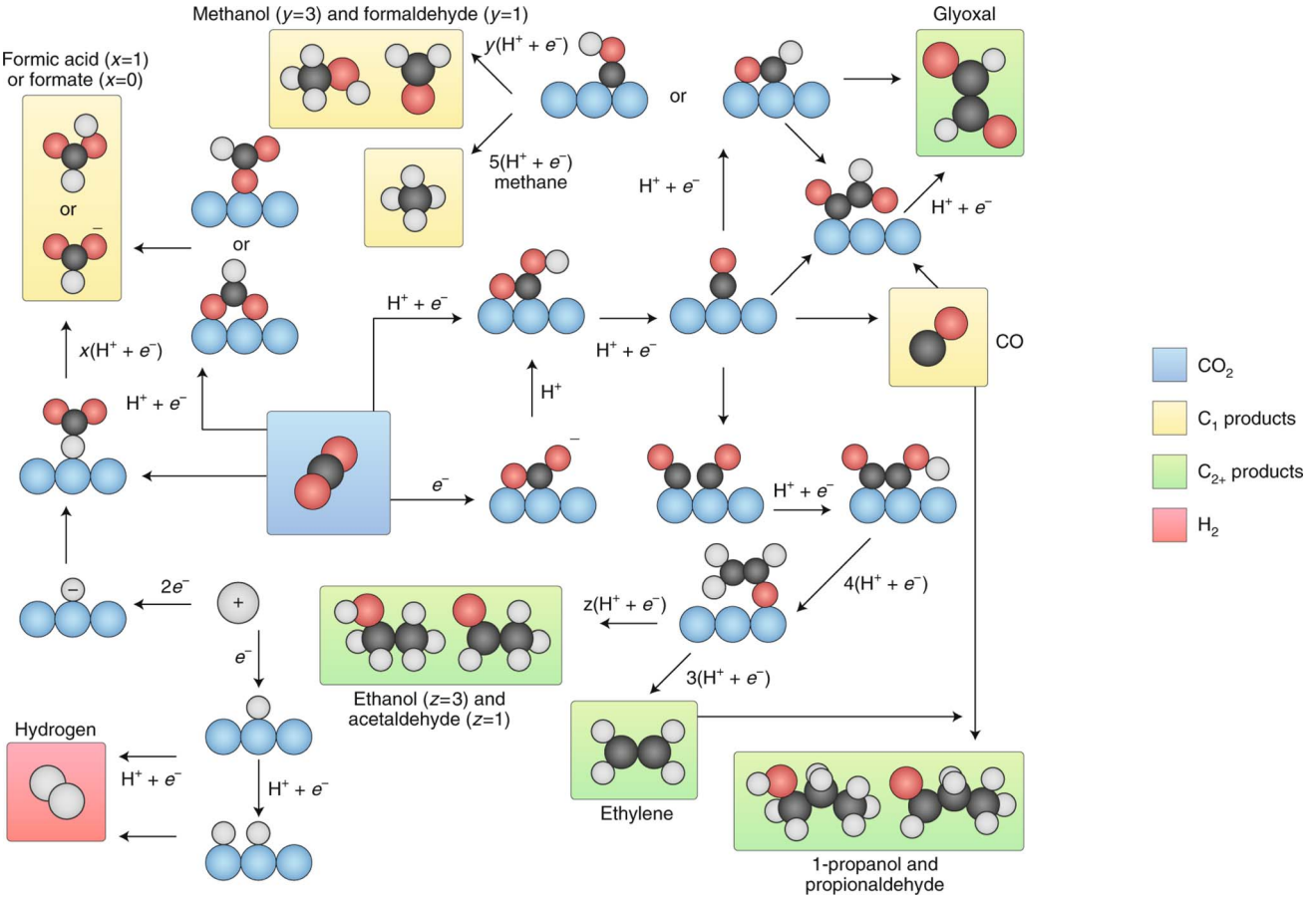

Fig. 13 Summary of the reaction pathways for the ECO_2RR leading to various products. Reproduced with permission.[123] Copyright 2019, Nature.

moment of M in M–B dual-atom sites promotes C–C coupling and protonation in the ECO_2RR under ambient conditions.

To elucidate why almost no DACs can efficiently produce substantial quantities of multi-carbon products, Li *et al.* conducted an in-depth examination of the surface states of representative homonuclear and heteronuclear DACs. They employed spin-polarized DFT calculations, incorporating van der Waals interactions, to explore the underlying mechanisms of the CO_2RR.[55] They discovered that the favorable surface states of DACs are covered by CO either unilaterally or bilaterally at the M–M bridge sites, making CO the primary product of DACs. However, C–C coupling predominantly occurs at the top sites of metal surfaces. However, CO tends to preferentially occupy the bridge sites between the two metal atoms. This preferential adsorption of CO at the bridge sites can hinder subsequent C–C coupling reactions. Furthermore, based on the energy changes, the occurrence of C–C coupling on the surface of DACs is both thermodynamically and kinetically unfeasible.

3.4. Electrochemical nitrogen reduction reaction

3.4.1. ENRR principles. In general, the electrocatalytic conversion of nitrogen to ammonia on a heterogeneous catalyst can proceed through three primary mechanisms: dissociative and associative pathways, each involving distinct intermediates, and the MvK pathway.[131] In the dissociation mechanism (Fig. 15a), the nitrogen molecule is separated into two nitrogen atoms when adsorbed on the catalyst, in which due to the inertia of the N≡N bond, the energy input is high before the hydrogenation reaction occurs, and the two separate nitrogen atoms are converted into each other by the hydrogenation process. Taking into account various sequences of H addition to N atoms, the hydrogenation process in the associative mechanism can follow three distinct pathways: distal, alternating, and enzymatic. As shown in Fig. 15b, in the distal pathway, one of the nitrogen atoms in a nitrogen molecule is connected to the active site of the catalyst, and the hydrogen process is carried out continuously from the N atom far away from the catalyst until the ammonia gas formed is separated, and then will continue to hydrogenate the nitrogen atom near the catalyst to generate a second ammonia molecule. In comparison, the alternating pathway also occurs in the end-on adsorption configuration, where a nitrogen atom is connected to the active site of the catalyst, but in the hydrogenation process, the two nitrogen atoms alternately bind hydrogen atoms until the final step of the pathway. In Fig. 15c, it can be seen that the enzymatic pathway occurs in a side-on adsorption configuration, in which the nitrogen molecule lies horizontally above the catalyst active site and two N atoms of N_2 are bonded to the catalytic active site simultaneously, and they alternately bind with H atoms until they release two NH_3 molecules.

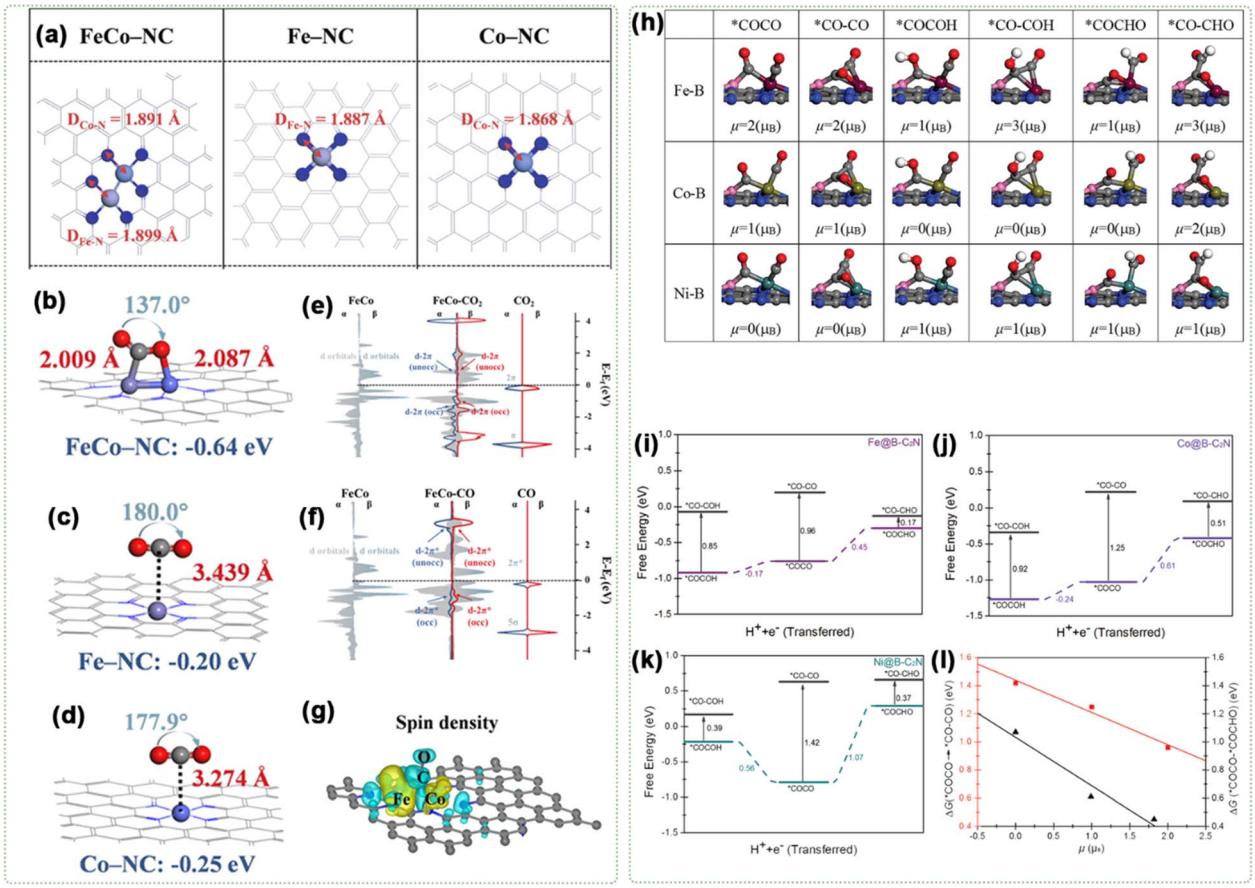

Fig. 14 (a) Optimized structural models. Predominant configurations of CO_2 adsorption for (b) FeCo–NC, (c) Fe–NC, and (d) Co–NC. Projected density of state (PDOS) analysis of (e) the 3d orbitals of Fe and Co dual-atom centers and the 2p orbitals of CO_2; (f) the 3d orbitals of Fe, Co dual-atom centers, 2p orbitals of the CO gas molecule. (g) Spin density of CO-assisted FeCo–NC. Reproduced with permission.[127] Copyright 2023, Wiley-VCH. (h) Optimized structure of C–C coupling. Free energy profiles for C–C coupling on (i) Fe@B-C_2N, (j) Co@B-C_2N, and (k) Ni@B-C_2N at 0 V (*vs.* RHE). (l) Correlation of the reaction free energy as a function of the spin moment (μ) for adsorbed reactants. Reproduced with permission.[130] Copyright 2021, Wiley-VCH.

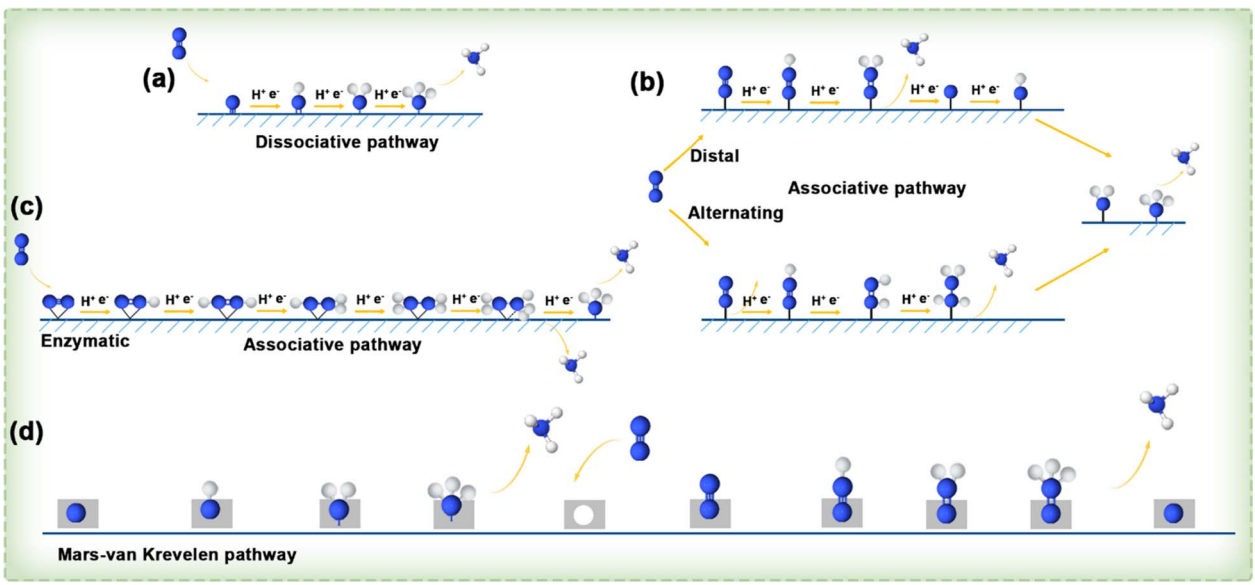

Fig. 15 (a–c) Diagram illustrating the dissociative and associative pathways. (d) Illustration depicting MvK reaction pathways.[131]

Additionally, a novel mechanism, entirely distinct from the dissociative and associative pathways, has been raised for the conversion of N_2 to NH_3, known as the MvK pathway. As illustrated in Fig. 15d, it is believed that NH_3 formation on the surface of transition metal nitrides (TMNs) follows this MvK pathway (or a combination of pathways including the MvK pathway). In accordance with this mechanism, N atoms in the TMN are reduced to NH_3, and the N_2 from the environment fills the vacancies left by the extracted lattice N atoms, thereby completing the catalyst renewal and preparing for a new reaction cycle.

3.4.2. Spin effect in the eNRR and eNO$_3$RR. NH_3 plays a crucial role in the production of fertilizers, as well as in the pharmaceutical and light industries.[132] The process of reducing nitrate to ammonia has attracted significant attention for the dual benefits of nitrate (NO_3^-) removal and ammonia (NH_3) production. Under low-temperature conditions, constructing an effective catalyst for the NRR is essential to achieve efficient large-scale NH_3 synthesis. Due to the cooperative effect and adjustable regulation of their dual-metal active sites, DACs can broaden the active configurational space, which is advantageous for complex multistep reactions, such as the NO_3RR.[133]

Zheng *et al.* discovered that Fe SA anchored on the oxide surface layer of Ti foam could improve the NH_3 Faradaic efficiency (FE). This enhancement was attributed to oxygen vacancies (OVs) in the titanium oxide layer, which cause spin polarization in both Fe and neighboring Ti atoms.[134] They confirmed the electronic structures and spin states of the spin-polarized Fe_1–Ti (SP-Fe_1–Ti) and spin-depressed Fe_1–Ti (SD-Fe_1–Ti) through various spectroscopic and magnetic measurements (Fig. 16a–f). DFT calculations were utilized to investigate the NITRR mechanism involving SP-Fe_1–Ti pairs. The spin density diagrams (Fig. 16g) show that in SD-Fe_1–Ti, only the Fe atom is spin-polarized. In contrast, both the Fe atom and the adjacent Ti atom are spin-polarized in the SP-Fe_1–Ti configuration. Additionally, in the SD-Fe_1–Ti configuration, the spin-up and spin-down components of the Ti atom are nearly equal. Nevertheless, the introduction of OVs leads to the emergence of unpaired electronic states near the E_F (Fig. 16h). The presence of magnetic Ti and Fe atoms plays a crucial role in enhancing the efficiency of the NITRR process. The primary interactions between Fe and NO arise from the $d_{xz}/d_{yz}/d_{z^2}$ orbitals of the Fe atom and the σ/π orbitals of NO (Fig. 16i), consistent with the high-spin-polarization configuration (t_{2g4} e_{g2}) of Fe. Consequently, the spin-polarized Fe–Ti paired sites could effectively facilitate NO^{3-} deoxygenation to *NO, stabilize *NO and *NHO intermediates, and enhance the subsequent *NO hydrogenation. This also inhibits the HER, resulting in a high activity and selectivity of the SP-Fe_1–Ti electrode for the NITRR. As anticipated, SP-Fe_1–Ti demonstrated outstanding performance, achieving an impressive NH_3 yield rate of 272 000 μg per h per mg per Fe with a high NH^3 FE of 95.2% at −0.4 V *vs.* RHE.

Zhang and colleagues designed and created a precisely defined Fe–Mo hetero-single-atom (h-SAs) electrocatalyst for the ENRR, which was obtained by co-anchoring atomically dispersed FeN_4 and MoN_4 coordination sites within a polyphthalocyanine (FeMoPPc) organic framework using a low-temperature melt polymerization technique.[135] ZFC *M–T* susceptibility measurements were performed to clarify the electronic configuration of the d-orbitals of Fe in FeMoPPc (Fig. 16j and k). The findings showed that the computed μ_{eff} values of the Fe sites for adsorption decreased from 2.43 to 1.89 μ_{eff}, following the incorporation of Mo. ^{57}Fe Mössbauer spectroscopy was performed and confirmed that the D1 peak could be attributed to FePc-like medium-spin $Fe^{II}N_4$ species, indicating that Fe^{II} was predominantly present in a medium-spin state in FeMoPPc through quantitative analysis (Fig. 16l). Notably altering the spin state of the Fe center from high spin to medium spin enhanced the π-backdonation process, aiding the initial hydrogenation of N_2. As expected, the energy barrier of the desorption of NH_3 on FeN_4 sites (0.09 eV) was much smaller than that on MoN_4 sites (0.54 eV). Consequently, the synthesized FeMoPPc with medium-spin FeN_4 demonstrated exceptional NRR performance. It showed faradaic efficiencies 2.0 and 9.0 times higher, and NH_3 yields 2.0 and 17.2 times greater than those of FePPc and MoPPc, respectively.

4. Summary and perspective

Significant attention has been directed toward controlling the spin states at the active centers of DACs. In this review, we delved into the implications of spin state transitions for various electrocatalytic reactions. We described the spin state transition characterizations and descriptors of atomic catalysts, and then proposed strategies for regulating the spin states of DACs' active centers. Finally, we summarized recent research on the spin effect of DACs in the ORR, OER, HER, ECO_2RR, and ENRR, providing a foundation for future studies. Despite progress, the research on spin state transitions in DACs is still in its early stage, and some key issues remain that deserve further attention, including the following:

(i) The impact of various spin states in DACs on different catalytic reactions remains under-researched. It is unclear whether spin state transitions alter the adsorption configurations of reaction intermediates and reaction pathways. In the future, more advanced characterization techniques need to be integrated to further probe the mechanisms.

(ii) Currently, the primary methods for studying spin state transitions in DACs rely on *ex situ* characterization techniques. During catalysis, the reaction intermediates adsorbed at active sites are dynamically evolving. *Ex situ* techniques cannot capture the spin state transitions of the magnetism of metal active centers during reaction processes. *In situ* characterization methods for detecting the spin states of active centers mainly include *in situ* Mössbauer spectroscopy and *in situ* XES. Advancing *in situ* characterization techniques for the real-time detection of spin states, such as *in situ* XAS and *in situ* VSM, is necessary for the on-site monitoring of the spin changes in active sites and reaction intermediates during catalytic reactions.

(iii) There exist limited approaches to modulate the spin states of the active centers of DACs. Additionally, there is a lack of real-time control strategies for spin states during reactions. The real-time regulation of spin states during reactions can help

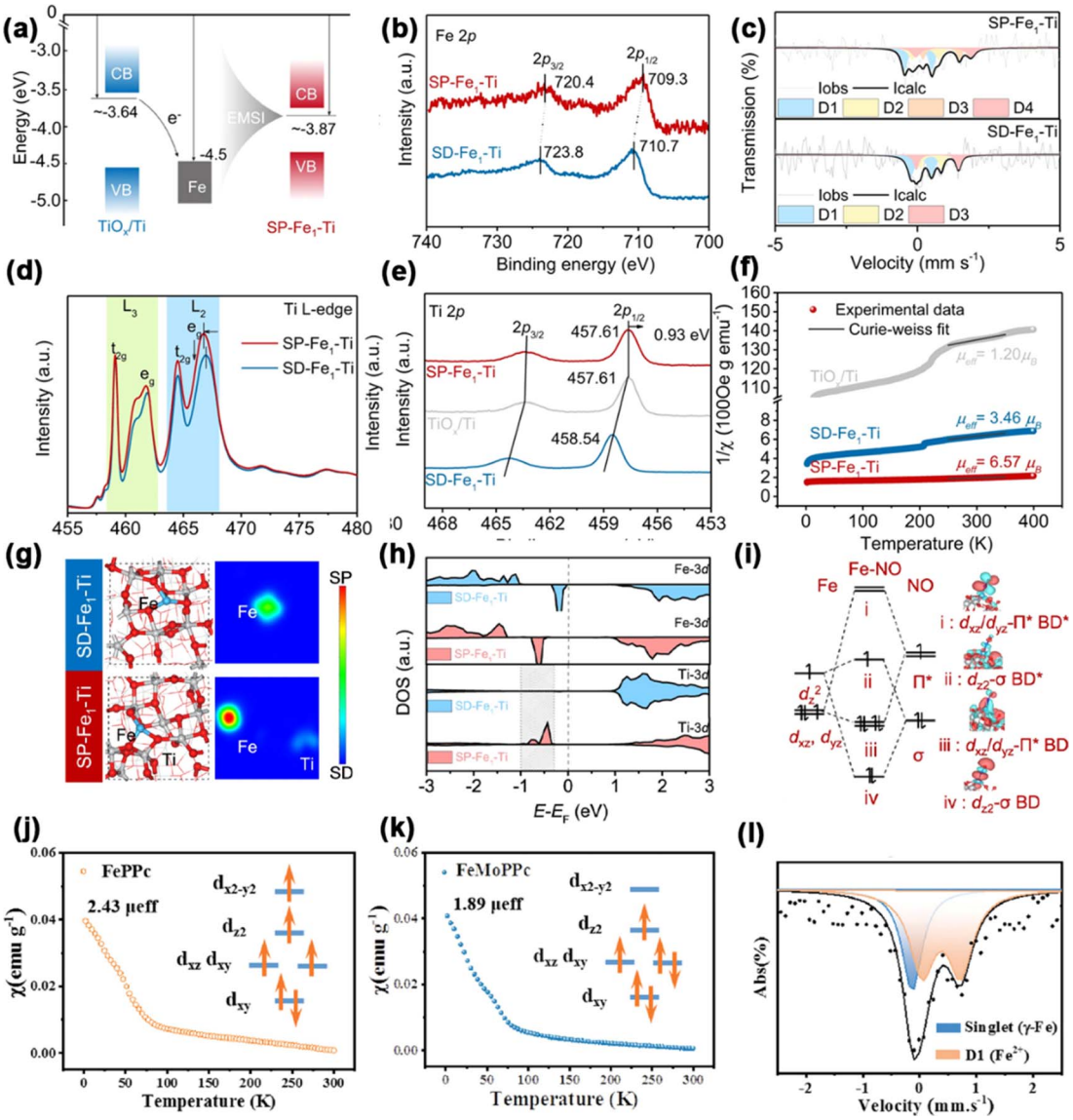

Fig. 16 (a) Energy alignment. (b) XPS spectra of Fe 2p; (c) Mössbauer spectra; (d) Ti L-edge soft-XAS spectra; (e) Ti 2p XPS spectra; (f) $1/\chi_m$ *versus* temperature plots and (g) optimized structures and spin density diagrams of SD-Fe$_1$–Ti and SP-Fe$_1$–Ti. (h) DOSs of Fe and Ti atoms. (i) Remarkable orbital interactions between the Fe atom and the NO molecule. Reproduced with permission.[134] Copyright 2024, Nature. Magnetic susceptibility of (j) FePPc and (k) FeMoPPc. (l) Room-temperature ^{57}Fe Mössbauer spectrum of FeMoPPc. Reproduced with permission.[135] Copyright 2024, Science.

optimize the adsorption and desorption of key reaction intermediates, thereby enhancing the catalyst function. Developing real-time spin state control strategies is a crucial research direction in this field.

(iv) The spin catalytic HER, ENRR, and ECO_2RR mechanisms on DACs are rarely reported. To develop more reliable electrocatalysts, it is essential to understand how changes in the spin states of their active centers affect their catalytic performances. Theoretical calculations using computational chemistry can not only assist experimental studies in identifying catalytic active sites, but can also play a crucial role in elucidating the reaction mechanisms, which in turn would help to guide the design of new catalysts. Therefore, future efforts are needed to address this challenge.

(v) Precise designs to take advantage of spin effects need to be explored. Additionally, there is no comprehensive summary on the selection of magnetic catalysts to achieve optimal catalytic performance. In the future, high-throughput theoretical calculations may be employed to analyze catalytic reaction mechanisms from the perspective of the electronic structure. Furthermore, machine learning could be utilized to elucidate the relationship between spin effects and performance, thereby guiding the design of catalysts.

In general, while prominent progress has been made in the spin effect of DACs in the field of electrocatalysis, several issues still need to be addressed. Nevertheless, we anticipate that the advancement of new synthesis methods, sophisticated characterization techniques, regulation strategies, and computational

theories will facilitate the rational design of high-performance DACs for energy-storage and -transformation applications.

Data availability

No primary research results, software or code has been included and no new data were generated or analysed as part of this review.

Author contributions

All of the authors contributed to the literature search, writing and editing of this review.

Conflicts of interest

There are no conflicts to declare.

Acknowledgements

This work was supported by the National Natural Science Foundation of China (No. 22075099), and the Natural Science Foundation of Jilin Province (No. 20220101051JC).

Notes and references

1 W. Zhang, Y. Chao, W. Zhang, J. Zhou, F. Lv, K. Wang, F. Lin, H. Luo, J. Li, M. Tong, E. Wang and S. Guo, *Adv. Mater.*, 2021, **33**, 2102576.
2 T. He, A. R. P. Santiago, Y. Kong, M. A. Ahsan, R. Luque, A. Du and H. Pan, *Small*, 2022, **18**, 2106091.
3 V. R. Stamenkovic, D. Strmcnik, P. P. Lopes and N. M. Markovic, *Nat. Mater.*, 2017, **16**, 57–69.
4 L. Tang, X. Meng, D. Deng and X. Bao, *Adv. Mater.*, 2019, **31**, 1901996.
5 Z. W. Seh, J. Kibsgaard, C. F. Dickens, I. Chorkendorff, J. K. Nørskov and T. F. Jaramillo, *Science*, 2017, **355**, eaad4998.
6 L. Xiao, Z. Wang and J. Guan, *Adv. Funct. Mater.*, 2024, **34**, 2310195.
7 L. Xiao, L. Qi, J. Sun, A. Husile, S. Zhang, Z. Wang and J. Guan, *Nano Energy*, 2024, **120**, 109155.
8 A. Wang, J. Li and T. Zhang, *Nat. Rev. Chem*, 2018, **2**, 65–81.
9 Y. Liu, L. Zhou, S. Liu, S. Li, J. Zhou, X. Li, X. Chen, K. Sun, B. Li, J. Jiang and H. Pang, *Angew. Chem., Int. Ed.*, 2024, **63**, e202319983.
10 B. Qiao, A. Wang, X. Yang, L. F. Allard, Z. Jiang, Y. Cui, J. Liu, J. Li and T. Zhang, *Nat. Chem.*, 2011, **3**, 634–641.
11 Y. Chen, S. Ji, C. Chen, Q. Peng, D. Wang and Y. Li, *Joule*, 2018, **2**, 1242–1264.
12 Z. Li, S. Ji, Y. Liu, X. Cao, S. Tian, Y. Chen, Z. Niu and Y. Li, *Chem. Rev.*, 2020, **120**, 623–682.
13 X. Bai, Y. Wang, J. Han, X. Niu and J. Guan, *Appl. Catal., B*, 2023, **337**, 122966.
14 Z. Zhang, C. Feng, D. Wang, S. Zhou, R. Wang, S. Hu, H. Li, M. Zuo, Y. Kong, J. Bao and J. Zeng, *Nat. Commun.*, 2022, **13**, 2473.
15 R. Li, J. Zhao, B. Liu and D. Wang, *Adv. Mater.*, 2024, **36**, 2308653.
16 Y. Hu, Z. Li, B. Li and C. Yu, *Small*, 2022, **18**, 2203589.
17 J. Zhang, Q.-a. Huang, J. Wang, J. Wang, J. Zhang and Y. Zhao, *Chin. J. Catal.*, 2020, **41**, 783–798.
18 T. Tang, X. Bai, Z. Wang and J. Guan, *Chem. Sci.*, 2024, **15**, 5082–5112.
19 R. R. Burch, E. L. Muetterties, R. G. Teller and J. M. Williams, *J. Am. Chem. Soc.*, 1982, **104**, 4257–4258.
20 C. Fang, J. Zhou, L. Zhang, W. Wan, Y. Ding and X. Sun, *Nat. Commun.*, 2023, **14**, 4449.
21 J. Wang, C.-X. Zhao, J.-N. Liu, Y.-W. Song, J.-Q. Huang and B.-Q. Li, *Nano Energy*, 2022, **104**, 107927.
22 T. Tang, Z. Wang and J. Guan, *Coord. Chem. Rev.*, 2023, **492**, 215288.
23 A. L. Buchachenko, L. V. Ruban, E. N. Step and N. J. Turro, *Chem. Phys. Lett.*, 1995, **233**, 315–318.
24 W. Zhang, K. Banerjee-Ghosh, F. Tassinari and R. Naaman, *ACS Energy Lett.*, 2018, **3**, 2308–2313.
25 Z. Fang, W. Zhao, T. Shen, D. Qiu, Y. Lv, X. Hou and Y. Hou, *Precis. Chem.*, 2023, **1**, 395–417.
26 G. Xu, C. Cai and T. Wang, *J. Am. Chem. Soc.*, 2022, **144**, 23089–23095.
27 F. A. Garcés-Pineda, M. Blasco-Ahicart, D. Nieto-Castro, N. López and J. R. Galán-Mascarós, *Nat. Energy*, 2019, **4**, 519–525.
28 X. Li, Z. Cheng and X. Wang, *Electrochem. Energy Rev.*, 2021, **4**, 136–145.
29 A. H. Compton, *J. Franklin Inst.*, 1921, **192**, 145–155.
30 D. Yardimci, P. Serna and B. C. Gates, *Chem.–Eur. J.*, 2013, **19**, 1235–1245.
31 J. Wang, Z. Huang, W. Liu, C. Chang, H. Tang, Z. Li, W. Chen, C. Jia, T. Yao, S. Wei, Y. Wu and Y. Li, *J. Am. Chem. Soc.*, 2017, **139**, 17281–17284.
32 Y. Sun, J. Wang, Q. Liu, M. Xia, Y. Tang, F. Gao, Y. Hou, J. Tse and Y. Zhao, *J. Mater. Chem. A*, 2019, **7**, 27175–27185.
33 H. Li, J. Wang, R. Qi, Y. Hu, J. Zhang, H. Zhao, J. Zhang and Y. Zhao, *Appl. Catal., B*, 2021, **285**, 119778.
34 G. Yang, J. Zhu, P. Yuan, Y. Hu, G. Qu, B.-A. Lu, X. Xue, H. Yin, W. Cheng, J. Cheng, W. Xu, J. Li, J. Hu, S. Mu and J.-N. Zhang, *Nat. Commun.*, 2021, **12**, 1734.
35 T. He, Y. Chen, Q. Liu, B. Lu, X. Song, H. Liu, M. Liu, Y.-N. Liu, Y. Zhang, X. Ouyang and S. Chen, *Angew. Chem., Int. Ed.*, 2022, **61**, e202201007.
36 J. Zhang, Y. Zhao, W. Zhao, J. Wang, Y. Hu, C. Huang, X. Zou, Y. Liu, D. Zhang, X. Lu, H. Fan and Y. Hou, *Angew. Chem., Int. Ed.*, 2023, **62**, e202314303.
37 L. Wang, Q. An, X. Sheng, Z. Mei, Q. Jing, X. Zhao, Q. Xu, L. Duan, X. Zou and H. Guo, *Appl. Catal., B*, 2024, **343**, 123509.
38 T. S. Metzger, S. Mishra, B. P. Bloom, N. Goren, A. Neubauer, G. Shmul, J. Wei, S. Yochelis, F. Tassinari, C. Fontanesi, D. H. Waldeck, Y. Paltiel and R. Naaman, *Angew. Chem., Int. Ed.*, 2020, **59**, 1653–1658.
39 K. Song, B. Yang, X. Zou, W. Zhang and W. Zheng, *Energy Environ. Sci.*, 2024, **17**, 27–48.

40 R. J. Soulen, J. M. Byers, M. S. Osofsky, B. Nadgorny, T. Ambrose, S. F. Cheng, P. R. Broussard, C. T. Tanaka, J. Nowak, J. S. Moodera, A. Barry and J. M. D. Coey, *Science*, 1998, **282**, 85–88.
41 R. G. Lawler, *J. Am. Chem. Soc.*, 1967, **89**, 5519–5521.
42 E. A. Zhukov, D. R. Yakovlev, A. Schwan, O. A. Yugov, A. Waag, L. W. Molenkamp and M. Bayer, *Phys. Status Solidi B*, 2014, **251**, 1872–1880.
43 B. F. Minaev and H. Ågren, *J. Quantum Chem.*, 1996, **57**, 519–532.
44 R. Chattot, O. Le Bacq, V. Beermann, S. Kühl, J. Herranz, S. Henning, L. Kühn, T. Asset, L. Guétaz, G. Renou, J. Drnec, P. Bordet, A. Pasturel, A. Eychmüller, T. J. Schmidt, P. Strasser, L. Dubau and F. Maillard, *Nat. Mater.*, 2018, **17**, 827–833.
45 H. Xue, J. Wang, H. Cheng, H. Zhang, X. Li, J. Sun, X. Wang, L. Lin, Y. Zhang, X. Liao and Y. He, *Appl. Catal., B*, 2024, **353**, 124087.
46 Y. Sun, H. Lv, H. Yao, Y. Gao and C. Zhang, *Carbon Energy*, 2024, e575.
47 X. Li and Z. Cheng, *Chem Catal.*, 2022, **2**, 2140–2149.
48 X. Li, C. Hao, Y. Du, Y. Lu, Y. Fan, M. Wang, N. Wang, R. Meng, X. Wang and Z. J. Xu, *Chin. J. Catal.*, 2023, **55**, 191–199.
49 S. Sun, Y. Zhang, X. Shi, W. Sun, C. Felser, W. Li and G. Li, *Adv. Mater.*, 2024, 2312524.
50 Y. Zhang, D. Wang, G. Wei, B. Li, Z. Mao, S.-M. Xu, S. Tang, J. Jiang, Z. Li, X. Wang and X. Xu, *JACS Au*, 2024, **4**, 1509–1520.
51 W. Zhong, Y. Qiu, H. Shen, X. Wang, J. Yuan, C. Jia, S. Bi and J. Jiang, *J. Am. Chem. Soc.*, 2021, **143**, 4405–4413.
52 P. Lv, W. Lv, D. Wu, G. Tang, X. Yan, Z. Lu and D. Ma, *Phys. Rev. Appl.*, 2023, **19**, 054094.
53 K. Liu, J. Fu, Y. Lin, T. Luo, G. Ni, H. Li, Z. Lin and M. Liu, *Nat. Commun.*, 2022, **13**, 2075.
54 Z. Li, Z. Wang, S. Xi, X. Zhao, T. Sun, J. Li, W. Yu, H. Xu, T. S. Herng, X. Hai, P. Lyu, M. Zhao, S. J. Pennycook, J. Ding, H. Xiao and J. Lu, *ACS Nano*, 2021, **15**, 7105–7113.
55 W. Yang, Z. Jia, B. Zhou, L. Chen, X. Ding, L. Jiao, H. Zheng, Z. Gao, Q. Wang and H. Li, *ACS Catal.*, 2023, **13**, 9695–9705.
56 H. Bai, J. Feng, D. Liu, P. Zhou, R. Wu, C. T. Kwok, W. F. Ip, W. Feng, X. Sui, H. Liu and H. Pan, *Small*, 2023, **19**, 2205638.
57 A. Cao and J. K. Nørskov, *ACS Catal.*, 2023, **13**, 3456–3462.
58 J. Huang, J. Yu, X. Lu, Y. Wei, H. Song, A. Cao, J. Cai, S.-Q. Zang and S. Lu, *Inorg. Chem. Front.*, 2023, **10**, 3955–3962.
59 L. Zhang and Z. Xia, *J. Phys. Chem. C*, 2011, **115**, 11170–11176.
60 M. Tamtaji, Q. Peng, T. Liu, X. Zhao, Z. Xu, P. R. Galligan, M. D. Hossain, Z. Liu, H. Wong, H. Liu, K. Amine, Y. Zhu, W. A. Goddard Iii, W. Wu and Z. Luo, *Nano Energy*, 2023, **108**, 108218.
61 Z. Zhang, Z. Xu, J. He and J. Lu, *IEEE Trans. Instrum. Meas.*, 2022, **71**, 1–9.
62 X. Li, Y. Sun, F. Ren, Y. Bai and Z. Cheng, *Mater. Today Energy*, 2021, **19**, 100619.
63 V. Shukla, *Introduction of Vibrating Sample Magnetometer for Magnetic Characterization*, Springer, Cham, 2022, pp. 483–505, DOI: **10.1007/978-3-030-90948-2_19**.
64 T. Kahmann, E. L. Rösch, K. Enpuku, T. Yoshida and F. Ludwig, *J. Magn. Magn. Mater.*, 2021, **519**, 167402.
65 S. Phokha, S. Pinitsoontorn, S. Maensiri and S. Rujirawat, *J. Sol-Gel Sci. Technol.*, 2014, **71**, 333–341.
66 H. Zhang, H.-C. Chen, S. Feizpoor, L. Li, X. Zhang, X. Xu, Z. Zhuang, Z. Li, W. Hu, R. Snyders, D. Wang and C. Wang, *Adv. Mater.*, 2024, **36**, 2400523.
67 Y. Liu, X. Liu, Z. Lv, R. Liu, L. Li, J. Wang, W. Yang, X. Jiang, X. Feng and B. Wang, *Angew. Chem., Int. Ed.*, 2022, **61**, e202117617.
68 Y. Li, Y. Ji, Y. Zhao, J. Chen, S. Zheng, X. Sang, B. Yang, Z. Li, L. Lei, Z. Wen, X. Feng and Y. Hou, *Adv. Mater.*, 2022, **34**, 2202240.
69 J. Ding, Z. Wei, F. Li, J. Zhang, Q. Zhang, J. Zhou, W. Wang, Y. Liu, Z. Zhang, X. Su, R. Yang, W. Liu, C. Su, H. B. Yang, Y. Huang, Y. Zhai and B. Liu, *Nat. Commun.*, 2023, **14**, 6550.
70 Z. Chen, H. Niu, J. Ding, H. Liu, P.-H. Chen, Y.-H. Lu, Y.-R. Lu, W. Zuo, L. Han, Y. Guo, S.-F. Hung and Y. Zhai, *Angew. Chem., Int. Ed.*, 2021, **60**, 25404–25410.
71 V. A. Saveleva, K. Ebner, L. Ni, G. Smolentsev, D. Klose, A. Zitolo, E. Marelli, J. Li, M. Medarde, O. V. Safonova, M. Nachtegaal, F. Jaouen, U. I. Kramm, T. J. Schmidt and J. Herranz, *Angew. Chem., Int. Ed.*, 2021, **60**, 11707–11712.
72 A. Brückner, *Chem. Soc. Rev.*, 2010, **39**, 4673–4684.
73 T. S. Seifert, S. Kovarik, D. M. Juraschek, N. A. Spaldin, P. Gambardella and S. Stepanow, *Sci. Adv.*, 2020, **6**, eabc5511.
74 M. Abbate, J. C. Fuggle, A. Fujimori, L. H. Tjeng, C. T. Chen, R. Potze, G. A. Sawatzky, H. Eisaki and S. Uchida, *Phys. Rev. B: Condens. Matter Mater. Phys.*, 1993, **47**, 16124–16130.
75 Y. Cao, L. Gao, Z. Lai, C. Wang, Y. Yao, X. Zhu and Z. Zou, *Appl. Phys. Lett.*, 2021, **119**, 163902.
76 X. Li, H. Liu, Z. Chen, Q. Wu, Z. Yu, M. Yang, X. Wang, Z. Cheng, Z. Fu and Y. Lu, *Nat. Commun.*, 2019, **10**, 1409.
77 X. Li, Y. Sun, Q. Wu, H. Liu, W. Gu, X. Wang, Z. Cheng, Z. Fu and Y. Lu, *J. Am. Chem. Soc.*, 2019, **141**, 3121–3128.
78 U. I. Kramm, M. Lefèvre, N. Larouche, D. Schmeisser and J.-P. Dodelet, *J. Am. Chem. Soc.*, 2014, **136**, 978–985.
79 J. Li, M. T. Sougrati, A. Zitolo, J. M. Ablett, I. C. Oğuz, T. Mineva, I. Matanovic, P. Atanassov, Y. Huang, I. Zenyuk, A. Di Cicco, K. Kumar, L. Dubau, F. Maillard, G. Dražić and F. Jaouen, *Nat. Catal.*, 2021, **4**, 10–19.
80 C. Chen, X. Zhu, X. Wen, Y. Zhou, L. Zhou, H. Li, L. Tao, Q. Li, S. Du, T. Liu, D. Yan, C. Xie, Y. Zou, Y. Wang, R. Chen, J. Huo, Y. Li, J. Cheng, H. Su, X. Zhao, W. Cheng, Q. Liu, H. Lin, J. Luo, J. Chen, M. Dong, K. Cheng, C. Li and S. Wang, *Nat. Chem.*, 2020, **12**, 717–724.
81 Y. Gao, J. Wang, Y. Yang, J. Wang, C. Zhang, X. Wang and J. Yao, *Nano-Micro Lett.*, 2023, **15**, 158.
82 X. Wang, L. Xu, C. Li, C. Zhang, H. Yao, R. Xu, P. Cui, X. Zheng, M. Gu, J. Lee, H. Jiang and M. Huang, *Nat. Commun.*, 2023, **14**, 7210.

83 L. Zhao, Q. Cai, B. Mao, J. Mao, H. Dong, Z. Xiang, J. Zhu, R. Paul, D. Wang, Y. Long, L. Qu, R. Yan, L. Dai and C. Hu, *Proc. Natl. Acad. Sci. U. S. A.*, 2023, **120**, e2308828120.
84 W. Zou, R. Lu, X. Liu, G. Xiao, X. Liao, Z. Wang and Y. Zhao, *J. Mater. Chem. A*, 2022, **10**, 9150–9160.
85 M. Liu, X. Wang, S. Cao, X. Lu, W. Li, N. Li and X.-H. Bu, *Adv. Mater.*, 2024, **36**, 2309231.
86 S. Ye, S. Xie, Y. Lei, X. Yang, J. Hu, L. Zheng, Z. Chen, Y. Fu, X. Ren, Y. Li, X. Ouyang, Q. Zhang, J. Liu and X. Sun, *Nano Res.*, 2023, **16**, 1869–1877.
87 T. Ding, X. Liu, Z. Tao, T. Liu, T. Chen, W. Zhang, X. Shen, D. Liu, S. Wang, B. Pang, D. Wu, L. Cao, L. Wang, T. Liu, Y. Li, H. Sheng, M. Zhu and T. Yao, *J. Am. Chem. Soc.*, 2021, **143**, 11317–11324.
88 M. Liu, S. Liu, Q. Xu, Q. Miao, S. Yang, S. Hanson, G. Z. Chen, J. He, Z. Jiang and G. Zeng, *Carbon Energy*, 2023, **5**, e300.
89 X. Sun, Y. Song, G. Jiang, X. Lan and C. Xu, *Sci. China Mater.*, 2024, **67**, 1–17.
90 P. Zhu, Z.-Y. Wu, A. Elgazzar, C. Dong, T.-U. Wi, F.-Y. Chen, Y. Xia, Y. Feng, M. Shakouri, J. Y. Kim, Z. Fang, T. A. Hatton and H. Wang, *Nature*, 2023, **618**, 959–966.
91 C. Cai, K. Liu, L. Zhang, F. Li, Y. Tan, P. Li, Y. Wang, M. Wang, Z. Feng, D. Motta Meira, W. Qu, A. Stefancu, W. Li, H. Li, J. Fu, H. Wang, D. Zhang, E. Cortés and M. Liu, *Angew. Chem., Int. Ed.*, 2023, **62**, e202300873.
92 J. Pei, L. Yang, J. Lin, Z. Zhang, Z. Sun, D. Wang and W. Chen, *Angew. Chem., Int. Ed.*, 2024, **63**, e202316123.
93 S. Biswas, J. Zhou, X.-L. Chen, C. Chi, Y.-A. Pan, P. Cui, J. Li, C. Liu and X.-H. Xia, *Angew. Chem., Int. Ed.*, 2024, **63**, e202405493.
94 L. Li, J. Zhu, F. Kong, Y. Wang, C. Kang, M. Xu, C. Du and G. Yin, *Matter*, 2024, **7**, 1517–1532.
95 G. Chen, Y. Sun, R. R. Chen, C. Biz, A. C. Fisher, M. P. Sherburne, J. W. Ager Iii, J. Gracia and Z. J. Xu, *J. Phys.: Energy*, 2021, **3**, 031004.
96 X. Li, Z. Cheng and X. Wang, *Electrochem. Energy Rev.*, 2021, **4**, 136–145.
97 H. He, S. Liu, Y. Liu, L. Zhou, H. Wen, R. Shen, H. Zhang, X. Guo, J. Jiang and B. Li, *Green Chem.*, 2023, **25**, 9501–9542.
98 K. Song, B. Yang, X. Zou, W. Zhang and W. T. Zheng, *Energy Environ. Sci.*, 2023, **17**, 27–48.
99 L. Han, H. Cheng, W. Liu, H. Li, P. Ou, R. Lin, H.-T. Wang, C.-W. Pao, A. R. Head, C.-H. Wang, X. Tong, C.-J. Sun, W.-F. Pong, J. Luo, J.-C. Zheng and H. L. Xin, *Nat. Mater.*, 2022, **21**, 681–688.
100 X. Han, T. Zhang, W. Chen, B. Dong, G. Meng, L. Zheng, C. Yang, X. Sun, Z. Zhuang and D. Wang, *Adv. Energy Mater.*, 2021, **11**, 2002753.
101 Y. Chen, J. Lin, B. Jia, X. Wang, S. Jiang and T. Ma, *Adv. Mater.*, 2022, **34**, 2201796.
102 T. Tang, Y. Wang, J. Han, Q. Zhang, X. Bai, X. Niu, Z. Wang and J. Guan, *Chin. J. Catal.*, 2023, **46**, 48–55.
103 C. Chen, Y. Li, A. Huang, X. Liu, J. Li, Y. Zhang, Z. Chen, Z. Zhuang, Y. Wu and W.-C. Cheong, *J. Am. Chem. Soc.*, 2023, **145**, 21273–21283.
104 H. Li, S. Di, P. Niu, S. Wang, J. Wang and L. Li, *Energy Environ. Sci.*, 2022, **15**, 1601–1610.
105 C. Wei, R. R. Rao, J. Peng, B. Huang, I. E. Stephens, M. Risch, Z. J. Xu and Y. Shao-Horn, *Adv. Mater.*, 2019, **31**, 1806296.
106 J. Fu, R. Liang, G. Liu, A. Yu, Z. Bai, L. Yang and Z. Chen, *Adv. Mater.*, 2019, **31**, 1805230.
107 X. Bai, J. Han, S. Chen, X. Niu and J. Guan, *Chin. J. Catal.*, 2023, **54**, 212–219.
108 F. Song, L. Bai, A. Moysiadou, S. Lee, C. Hu, L. Liardet and X. Hu, *J. Am. Chem. Soc.*, 2018, **140**, 7748–7759.
109 X. Zhu, D. Zhang, C.-J. Chen, Q. Zhang, R.-S. Liu, Z. Xia, L. Dai, R. Amal and X. Lu, *Nano Energy*, 2020, **71**, 104597.
110 S. Sarkar, A. Biswas, E. E. Siddharthan, R. Thapa and R. S. Dey, *ACS Nano*, 2022, **16**, 7890–7903.
111 L. Bai, C.-S. Hsu, D. T. Alexander, H. M. Chen and X. Hu, *Nat. Energy*, 2021, **6**, 1054–1066.
112 T. Tang, J. Han, Z. Wang, X. Niu and J. Guan, *Nano Res.*, 2024, **17**, 3794–3800.
113 T. Tang, Z. Duan, D. Baimanov, X. Bai, X. Liu, L. Wang, Z. Wang and J. Guan, *Nano Res.*, 2023, **16**, 2218–2223.
114 W. Wan, Y. Zhao, S. Wei, C. A. Triana, J. Li, A. Arcifa, C. S. Allen, R. Cao and G. R. Patzke, *Nat. Commun.*, 2021, **12**, 5589.
115 J. Zhang, Y. Zhao, W. Zhao, J. Wang, Y. Hu, C. Huang, X. Zou, Y. Liu, D. Zhang and X. Lu, *Angew. Chem., Int. Ed.*, 2023, **62**, e202314303.
116 K. Yuan, D. Lützenkirchen-Hecht, L. Li, L. Shuai, Y. Li, R. Cao, M. Qiu, X. Zhuang, M. K. Leung and Y. Chen, *J. Am. Chem. Soc.*, 2020, **142**, 2404–2412.
117 B. Hu, A. Huang, X. Zhang, Z. Chen, R. Tu, W. Zhu, Z. Zhuang, C. Chen, Q. Peng and Y. Li, *Nano Res.*, 2021, **14**, 3482–3488.
118 Y. Shi and B. Zhang, *Chem. Soc. Rev.*, 2016, **45**, 1529–1541.
119 F. Sun, Q. Tang and D.-e. Jiang, *ACS Catal.*, 2022, **12**, 8404–8433.
120 L. Wan, Z. Xu, Q. Xu, M. Pang, D. Lin, J. Liu and B. Wang, *Energy Environ. Sci.*, 2023, **16**, 1384–1430.
121 Y. Chen, K. Yang, B. Jiang, J. Li, M. Zeng and L. Fu, *J. Mater. Chem. A*, 2017, **5**, 8187–8208.
122 W. Zhang, Y. Hu, L. Ma, G. Zhu, Y. Wang, X. Xue, R. Chen, S. Yang and Z. Jin, *Adv. Sci.*, 2018, **5**, 1700275.
123 Y. Y. Birdja, E. Pérez-Gallent, M. C. Figueiredo, A. J. Göttle, F. Calle-Vallejo and M. T. Koper, *Nat. Energy*, 2019, **4**, 732–745.
124 J. Han, X. Bai, X. Xu, A. Husile, S. Zhang, L. Qi and J. Guan, *Chem. Sci.*, 2024, **15**, 7870–7907.
125 F. Li, A. Thevenon, A. Rosas-Hernández, Z. Wang, Y. Li, C. M. Gabardo, A. Ozden, C. T. Dinh, J. Li and Y. Wang, *Nature*, 2020, **577**, 509–513.
126 J. E. Huang, F. Li, A. Ozden, A. Sedighian Rasouli, F. P. García de Arquer, S. Liu, S. Zhang, M. Luo, X. Wang and Y. Lum, *Science*, 2021, **372**, 1074–1078.
127 S. Cao, S. Zhou, H. Chen, S. Wei, S. Liu, X. Lin, X. Chen, Z. Wang, W. Guo and X. Lu, *Energy Environ. Mater.*, 2023, **6**, e12287.

128 Z. Jin, M. Yang, Y. Dong, X. Ma, Y. Wang, J. Wu, J. Fan, D. Wang, R. Xi and X. Zhao, *Nano-Micro Lett.*, 2024, **16**, 4.
129 X. Kong, J. Ke, Z. Wang, Y. Liu, Y. Wang, W. Zhou, Z. Yang, W. Yan, Z. Geng and J. Zeng, *Appl. Catal., B*, 2021, **290**, 120067.
130 M. He, W. An, Y. Wang, Y. Men and S. Liu, *Small*, 2021, **17**, 2104445.
131 X. Zhao, G. Hu, G. F. Chen, H. Zhang, S. Zhang and H. Wang, *Adv. Mater.*, 2021, **33**, 2007650.
132 Y. Ashida, K. Arashiba, K. Nakajima and Y. Nishibayashi, *Nature*, 2019, **568**, 536–540.
133 X. Lv, W. Wei, B. Huang, Y. Dai and T. Frauenheim, *Nano Lett.*, 2021, **21**, 1871–1878.
134 J. Dai, Y. Tong, L. Zhao, Z. Hu, C.-T. Chen, C.-Y. Kuo, G. Zhan, J. Wang, X. Zou and Q. Zheng, *Nat. Commun.*, 2024, **15**, 88.
135 Y. Wang, W. Cheng, P. Yuan, G. Yang, S. Mu, J. Liang, H. Xia, K. Guo, M. Liu, S. Zhao, G. Qu, B.-A. Lu, Y. Hu, J. Hu and J.-N. Zhang, *Adv. Sci.*, 2021, **8**, 2102915.